4-17-2018

Simulations of hydrogel-coated neural microelectrodes to assess biocompatibility improvement using strain as a metric for micromotion

Sarah A. Bentil
Iowa State University, sbentil@iastate.edu

Rebecca B. Dupaix
The Ohio State University

Simulations of hydrogel-coated neural microelectrodes to assess biocompatibility improvement using strain as a metric for micromotion

Abstract

This study investigates the benefit of coating silicon-substrate microelectrode arrays with hydrogel material for improved biocompatibility. Varying coating thicknesses and hydrogel material descriptions were considered to determine the impact on reducing strain in the surrounding brain tissue caused by relative micromotion of the electrode. Finite element simulations were used to explore biocompatibility by focusing on the longitudinal micromotion of an implanted single electrode shank. The finite element model for the brain and electrode, both with and without the hydrogel coating, remained constant. Three constitutive models were considered to describe the brain and/or hydrogel material: linear elastic, hyperviscoelastic, and fractional Zener. All combinations of these three material descriptions were explored. The simulation results showed that the constitutive model, electrode coating thickness, and the degree of microelectrode adhesion to the brain influenced the maximum principal logarithmic strain and also the maximum electrode displacement. Biocompatibility was improved as evidenced by a reduction in the magnitude of strain in the brain when (i) a hydrogel coating was applied to the silicon electrode, (ii) the thickness of the hydrogel coating was increased, and (iii) the brain adhered completely to the hydrogel coating. A decrease in microelectrode displacement may be a useful metric for assessing an improvement in micromotion reduction.

Keywords

finite element method, neural prosthetics, biocompatibility, biological tissues, hydrogels, electrodes, fractional Zener

Comments

This is the version of the article before peer review or editing, as submitted by an author to *Biomedical Physics & Engineering Express*. IOP Publishing Ltd is not responsible for any errors or omissions in this version of the manuscript or any version derived from it. The Version of Record is available online at DOI: 10.1088/2057-1976/aab990.

Simulations of Hydrogel-coated Neural Microelectrodes to Assess Biocompatibility Improvement using Strain as a Metric for Micromotion

Sarah A. Bentil[a,*], Rebecca B. Dupaix[b]

[a]*Department of Mechanical Engineering, Iowa State University of Science and Technology, 2529 Union Drive, Ames, IA 50011, USA*
[b]*Department of Mechanical and Aerospace Engineering, The Ohio State University, 201 West 19th Avenue, Columbus, OH 43210, USA*

Abstract

This study investigates the benefit of coating silicon-substrate microelectrode arrays with hydrogel material for improved biocompatibility. Varying coating thicknesses and hydrogel material descriptions were considered to determine the impact on reducing strain in the surrounding brain tissue caused by relative micromotion of the electrode. Finite element simulations were used to explore biocompatibility by focusing on the longitudinal micromotion of an implanted single electrode shank. The finite element model for the brain and electrode, both with and without the hydrogel coating, remained constant. Three constitutive models were considered to describe the brain and/or hydrogel material: linear elastic, hyperviscoelastic, and fractional Zener. All combinations of these three material descriptions were explored. The simulation results showed that the constitutive model, electrode coating thickness, and the degree of microelectrode adhesion to the brain influenced the maximum principal logarithmic strain and also the maximum electrode displacement. Biocompatibility was improved as evidenced by a reduction in the magnitude of strain in the brain when (i) a hydrogel coating was applied to the silicon electrode, (ii) the thickness of the hydrogel coating was increased, and (iii) the brain adhered completely to the

*Corresponding author:
Email address: sbentil@iastate.edu (Sarah A. Bentil)
URL: www.me.iastate.edu/sbentil/ (Sarah A. Bentil)

hydrogel coating. A decrease in microelectrode displacement may be a useful metric for assessing an improvement in micromotion reduction.
Keywords: finite element method, neural prosthetics, biocompatibility, biological tissues, hydrogels, electrodes

---

1. Introduction

Neural prostheses are used clinically in many medical applications, including sensory functions and motor functions (Maharbiz et al., 2017; Cheung, 2007; Hochberg et al., 2006; Rousche and Normann, 1992; Winter et al., 2007). Patients afflicted with movement disorders, such as tremor in Parkinson's disease, can opt for the deep brain stimulation (DBS) surgical procedure, which implants neural electrodes in the targeted brain region and places the device that powers the electrode in the chest area (Breit et al., 2004). To ensure that the targeted brain area is identified by the neurosurgeons, the DBS surgical procedure can be performed while the patient is fully awake.

The neural prostheses consist of metal electrodes (e.g., gold, iridium) that can be supported on silicon substrates or polymer-based substrates, such as polyimide (Maharbiz et al., 2017; Cutrone et al., 2015; Green et al., 2008; Kim et al., 2004; Polikov et al., 2005). The Young's modulus for silicon-substrates and polyimide is 165 GPa and 3 GPa, respectively (Maharbiz et al., 2017; Lee et al., 2005; Subbaroyan et al., 2005). The stiff silicon substrates are more commonly used for microfabricating the electrodes due to established processing techniques, although it is a brittle material compared with the flexible and biocompatible polyimide (Cutrone et al., 2015; Cheung et al., 2007; Subbaroyan et al., 2005).

On October 25, 2015, the National Geographic Channel in partnership with Mental Floss aired a live video on U.S. television and globally in 171 countries of a patient with Parkinson-related tremors receiving the DBS surgery (NGC, 2015). The surgery was a success; however, both short and long-term problems can arise due to adverse interactions between the brain tissue and the implant

such as nerve degeneration and inflammation (Jorfi et al., 2015; Polikov et al., 2006). One source of these problems is the mechanical mismatch between the implanted materials and neural tissue, which is complicated by relative micromotion between the brain tissue and the more rigid electrode material (Xiang et al., 2016). The long-term performance of these electrodes can be increased by using conducting polymer coatings, which have been shown to improve the biocompatibility of the electrode as compared with its silicon-substrate counterpart (Jorfi et al., 2015; Grill et al., 2009; Harris et al., 2013; Kim et al., 2010).

Lee et al. (2005) applied the finite element (FE) method to investigate the magnitude and distribution of strain around a single silicon electrode shank that has been implanted in the brain. The effect of the strain field due to varying degrees of coupling between the silicon electrode and the brain tissue and different micromotion directions were also considered in the study by (Lee et al., 2005). A prediction that application of a neuro-integrative coatings on the silicon electrodes would decrease the total strain present in the brain was made by Lee et al. (2005) without much detail. Our work expands on this prediction by considering a FE model of a biocompatible hydrogel-coated silicon electrode and the conditions that will yield a reduction of the inherent relative micromotion and strain, for improved long term effectiveness. The hydrogel coating used in the FE analysis is assumed to be conductive with mechanical properties that mimic neural tissue.

Manufacturing hydrogel-coated electrodes is possible since conducting polymers can be electrochemically grown on hydrogel scaffolds having mechanical properties that are designed to mimic brain tissue (Kim et al., 2004). The integration of conducting polymers with hydrogels maintains the electrical functionality of the electrode, while improving biocompatibility (Harris et al., 2013).

Green et al. (2012) developed a protocol for synthesizing these biocompatible conducting hydrogels with electroactivity comparable to metal electrodes. Hassarati et al. (2014) showed that the use of a biocompatible conducting hydrogel coating minimized scar tissue formation and fluid accumulation, which improved the electrical performance of the interface between the tissue and neu-

ral electrode.

Although silicon and polyimide-based substrates used for the neural electrodes differ mechanically, one study (Subbaroyan et al., 2005) showed that they both produced similar strain profiles in brain tissue due to longitudinal micromotion. Thus, silicon-substrate electrodes were considered for this work. A FE model was used to examine the effect of coating the rigid silicon electrodes with varying soft hydrogel coating thicknesses. The effects of coating stiffness and adhesion on strain reduction were also studied. For simplicity, the FE model ignored the swelling ratios of hydrogels, which impact the pressure exerted on the brain tissue. The antifouling nature of hydrogels which resist adherence to surrounding tissues was also not considered in the FE model since Rao et al. (2011) developed a technique and showed that an increase in the hydrogel's ability to adhere to neural tissue can be obtained by synthesizing polylysine-modified poly(ethylene glycol) (PEG)-based hydrogels. The linear elastic (LE), hyperviscoelastic (HV), which is a combination of hyperelastic and linear viscoelastic (Miller, 1999), and fractional Zener (FZ) (Bentil and Dupaix, 2014; Davis et al., 2006) constitutive models were used to describe the mechanical properties of both the brain tissue and hydrogel coating in the FE simulations. For strain in the brain that is less than 5%, the LE model can be considered over biofidelic constitutive models due to its simplicity in implementation of the linear stress-strain response (Bentil and Dupaix, 2014; Miller, 1999). The LE constitutive model can capture the elastic behavior of the brain tissue, but is limited in its ability to accurately describe the non-linear response of the brain at higher strains and for varying strain-rates. Hyperelastic models can capture the nonlinear stress-strain relationship of the brain tissue due to an external load, such as compression, but not the strain-rate dependence of the brain tissue. Viscoelastic constitutive models (e.g. FZ and HV) contain both elastic and viscous components, which are needed to describe the brain's nonlinear stress-strain response, strain-rate dependent properties, and hysteresis. Thus, the FZ or HV constitutive model is ideal to accurately model the mechanical response of brain tissue and hydrogel coating, when compared to a

linear elastic or hyperelastic constitutive model. The silicon portion of the electrode was modeled throughout using a linear elastic material model to describe the mechanical behavior.

The results of this work will add to the sparse body of experimental and modeling literature for soft biological tissues. Furthermore, it can be used to develop a robust system model for the fabrication of a prototype hydrogel-coated neural electrode implant.

2. Method and Theory

Finite element simulations were performed using the software package ABAQUS CAE (ABAQUS, 2011) to simulate the effect of electrode coating thickness on reducing the strain present in the cerebral cortex. The FE simulations focused on the implanted electrode and also the region of the cortex closest to this electrode tip. To reduce computational time, only a quarter symmetric section of the brain-electrode aggregate was modeled.

2.1. Constitutive Model Coefficients

Linear elastic properties applied in our FE model for the brain and silicon-substrate electrode were provided by Lee et al. (2005). Simulations involving optimized linear elastic constants using low strain rate pig brain experimental data from Bentil (2013) were also performed. The linear elastic constants of the nearly incompressible brain described in the study of Lee et al. (2005) had a Young's modulus of 15 kPa and a Poisson's ratio of 0.49. A Young's modulus of 1696 Pa and a Poisson's ratio of 0.49 were the optimized linear elastic coefficients for pig brains using data from Bentil (2013). The aforementioned linear elastic material constants for the brain tissue were also used when describing the LE hydrogel coating, in our work. The silicon-substrate electrode material constants had a Young's modulus and Poisson's ratio of 165 GPa and 0.22, respectively (Lee et al., 2005). In all simulations, the silicon-substrate electrode was assumed to behave linear elastically.

Assuming that the brain is an isotropic material, a relationship between the Young's modulus and initial shear modulus can be made using Poisson's ratio. The calculated shear modulus for the porcine brain using Bentil (2013) constants and equation (1) is 0.57 kPa. This value is comparable to reported initial shear modulus values in the literature for low strain rate experiments on pig brains, which range between 0.2 kPa - 1.8 kPa (Donnelly and Medige, 1997; Miller and Chinzei, 2002; Prange and Margulies, 2002).

$$\mu_0 = \frac{E}{2\,(1+\nu)}, \tag{1}$$

where μ_0 is the shear modulus, E is the Young's modulus, and ν is Poisson's ratio.

Miller (1999) applied their hyperviscoelastic (HV) constitutive model to describe the mechanical behavior of swine brain tissue at low strain rates. They also used an axisymmetric two-dimensional (2D) finite element model to simulate swine brain being subjected to unconfined compression tests. The analysis for our study required three-dimensional (3D) elements. Verification was performed, prior to application of the HV model with the brain-electrode finite element analysis, to ensure that application of this constitutive model using 3D elements would yield the same results as the 2D case. Table 1 lists the material properties used to describe the brain when the HV constitutive model was considered. These constants were also applied to the hydrogel coating for the HV case.

Table 1: Coefficients for the hyperviscoelastic (HV) material model used to describe the brain and/or hydrogel coating provided by Miller (1999).

Hyperelastic	Viscoelastic	
$C_{100} = C_{010} = 263$ (Pa)	$t_1 = 0.5$ (s)	$t_2 = 50$ (s)
$C_{200} = C_{020} = 491$ (Pa)	$g_1 = 0.450$	$g_2 = 0.365$
$C_{110} = 0$ (Pa)	$k_1 = 0$	$k_2 = 0$
$D_1 = D_2 = 0$		

The hyperelastic constants C_{100}, C_{200}, and C_{110} describe the instantaneous elasticity of the material, while the D_1 parameter introduces compressibility into the model if volumetric test data is available. The time dependent behavior is described by the viscoelastic parameters of table 1. These parameters include two time constants (t_1 and t_2), relaxation coefficients (g_1 and g_2), and bulk coefficients (k_1 and k_2) that are set to the value zero due to the assumption of incompressibility.

Implementation of the 3D FZ model in ABAQUS is based on the work by Enelund et al. (1999) and Gil-Negrete et al. (2009). A user defined subroutine (UMAT) was written using the software FORTRAN to describe the FZ constitutive model. The algorithm required the decomposition of the stress and strain tensors into their volumetric and deviatoric parts. Additional details of the UMAT algorithm for the FZ model can be found in Appendix A. The coefficients of the FZ constitutive model for the brain were obtained from a previous study by Bentil and Dupaix (2014). These FZ material constants are provided in table 2 and were also applied to the hydrogel coating. The elastic property is captured by the coefficient E. The relaxation time is described by the parameter τ. The fractional order (α) ranges between 0 and 1 for a viscoelastic material (Bentil and Dupaix, 2014).

Table 2: Coefficients for the fractional Zener (FZ) material model used to describe the brain and/or hydrogel coating and other constants needed to implement the UMAT (Bentil and Dupaix, 2014).

Fractional Zener	
E_∞	442 (Pa)
E_0	3520 (Pa)
τ_0	7.62 (s)
$\alpha_{volumetric}$	0.624
$\alpha_{deviatoric}$	0.624
Poisson's ratio (ν)	0.49
θ^*	0.5
$c_0(\alpha)^{**}$	1

* θ specifies the implicitness of the integration in general form.

** c_0 is the initial coefficient from truncation of Grünwald's algorithm of differential-integration and is a function of α.

2.2. Geometry of the Brain and Electrode

Two different geometries were modeled for the FE simulations: brain and electrode. The length, width, and height of the brain geometry was 1.5 mm, 1.5 mm, and 7.5 mm, respectively. For the present paper, FE simulations of the electrode focused on only a single shank of the Michigan probe/electrode. The Michigan probe/electrode (Drake et al., 1988; Hetke and Anderson, 2003) is a commonly used silicon-substrate microelectrode array for chronic unit recording in the cerebral cortex (Kipke et al., 2003; Lee et al., 2005). The shank of the Michigan probe is the portion of the electrode that would be inserted into the brain tissue. The geometry and dimensions of the shank are illustrated in figure 1 and were obtained from Lee et al. (2005). For simulations with a hydrogel-coated shank (electrode), a single part consisting of the combined electrode and coating geometry was modeled. This single part was then partitioned to yield

two regions describing the silicon-substrate electrode and hydrogel coating geometry. Partitioning the combined electrode and coating geometry facilitated the creation of a coating region on all of the external lateral surfaces of the electrode; for the quarter-symmetric model shown in figure 1(b), this meant that the left and back surfaces has a uniform-thickness coating created on the outside of the electrode at the desired thickness. Appropriate constitutive models where then applied to the electrode and coating region. In all simulations involving hydrogel-coated electrodes, it is assumed that the coating has completely adhered to the electrode (bonded case).

Kim et al. (2004, 2010) have successfully produced uniformly coated hydrogel layers along the shank of the electrode probe with coating thickness ranging between 5 μm and 200 μm. Using those values as a guideline, coupled with the fact that acute injury increases with coating thickness, the finite element simulations considered five coating thicknesses (5 μm, 10 μm, 20 μm, 40 μm, and 80 μm). The maximum coating thickness of 80 μm was selected since one study showed that a coating thickness greater than 100 μm led to oxygen deprivation of the growing neurons (Kim et al., 2004). Furthermore, recording quality was not affected by the thickness of the hydrogel coating if the coating thickness was under 100 μm (Kim et al., 2004, 2010).

2.3. Mesh and Analysis Procedure

FE simulations using either a linear elastic or FZ constitutive model to describe the material behavior of the brain and/or electrode coating were modeled using 10-node quadratic tetrahedron (C3D10) and 20-node quadratic brick (C3D20) elements. A 10-node quadratic tetrahedron, hybrid, constant pressure element (C3D10H) was used to describe brain tissue defined as hyperviscoelastic (HV). A 20-node quadratic brick, hybrid, linear pressure element (C3D20H) was used when the FE simulation considered a HV hydrogel coating. Since the HV constitutive model includes a hyperelastic component, hybrid elements were used to account for the nearly incompressible assumption for the brain and/or electrode coating.

Figure 1 illustrates the mesh used for both the brain and electrode.

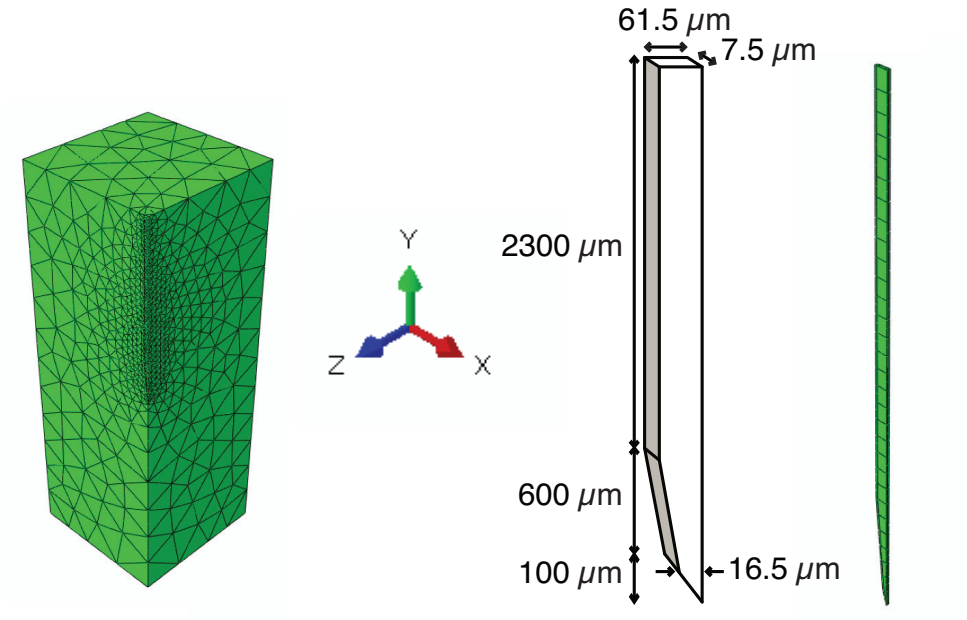

(a) (b)

Figure 1: (a) Mesh of the quarter symmetric brain. (b) Schematic of the uncoated silicon electrode shank (left) and corresponding mesh (right). Dimensions of the shank were obtained from Lee et al. (2005). Loads are applied to the longitudinal direction (negative "Y" direction) of the electrode shank, for simplicity in the FE model.

A "static, general" analysis procedure was used for all combinations of brain-electrode models with material behavior classified as LE or FZ. Any simulation requiring the use of the HV material to describe the brain or hydrogel coating required the "visco" analysis procedure due to the inclusion of the viscoelastic material properties. Nonlinear geometric effects were included for all simulations.

2.4. Notation

Different combinations of constitutive models were possible to describe the brain tissue and electrode, both with and without a hydrogel coating. Table 3

highlights all possible combinations. The nomenclature for the brain-electrode-coating system is as follows: the first two characters describe the model used for the brain tissue. The next two characters describe the silicon-substrate electrode and, if present, the final two characters indicate the material model used for the coating.

Table 3: Nomenclature to describe the constitutive model applied to the brain, electrode, and hydrogel coating.

Notation	Description
FZ-Si	Fractional Zener brain with silicon electrode (no coating)
FZ-SiFZ	Fractional Zener brain with silicon electrode and fractional Zener coating
FZ-SiHV	Fractional Zener brain with silicon electrode and hyperviscoelastic coating
FZ-SiLE	Fractional Zener brain with silicon electrode and linear elastic coating
HV-Si	Hyperviscoelastic brain with silicon electrode (no coating)
HV-SiFZ	Hyperviscoelastic brain with silicon electrode and fractional Zener coating
HV-SiHV	Hyperviscoelastic brain with silicon electrode and hyperviscoelastic coating
HV-SiLE	Hyperviscoelastic brain with silicon electrode and linear elastic coating
LE-Si	Linear elastic brain with silicon electrode (no coating)
LE-SiFZ	Linear elastic brain with silicon electrode and fractional Zener coating
LE-SiHV	Linear elastic brain with silicon electrode and hyperviscoelastic coating
LE-SiLE	Linear elastic brain with silicon electrode and linear elastic coating

2.5. Surface Interaction Properties Describing Adhesive Behavior

Varying degrees of physical coupling between the surfaces of the coated and uncoated electrode and brain were simulated to understand the effect of adhesion on micromotion reduction. The case of nonexistent adhesion between the electrode (coated/uncoated) and the brain was achieved by using a frictionless interface between the electrode (coated/uncoated) and the brain tissue. A linear pressure-overclosure was assumed for the normal behavior, with a contact stiffness of 0.00483. The contact stiffness value was obtained by adjusting the

LE-Si finite element model such that the displacements obtained were comparable with the results presented by Lee et al. (2005).

The same normal behavior described for the frictionless case was employed with the friction coefficients (μ) ranging from 0.5 to 1.0. The tangential behavior selected was a penalty friction formulation with an elastic slip tolerance value of 0.85. Increasing the friction coefficient simulated an increase of physical coupling between the brain tissue and the electrode (coated/uncoated). To simulate a fully bonded case between the electrode (coated/uncoated) and brain, a friction formulation was applied for the tangential behavior. The normal behavior for these simulations considered a "hard" contact pressure-overclosure where separation of the brain and electrode after contact was not allowed. A penalty constraint was enforced using linear contact behavior with the same stiffness value as the frictionless case.

2.6. Application of Load

The mechanical properties of the electrode must be stiff enough to survive the forces it will experience during the insertion procedure. This may be achieved by using a biocompatible polymer which dissolves in water, but is solid at room temperature (Cheung, 2007). Therefore, the coating on the silicon-substrate would begin as a rigid polymer and soften into a hydrogel after implantation. The load application for our analysis was the same as that published by Lee et al. (2005). Thus, it is assumed that the electrode has already been implanted into the cerebral cortex. All loads are then applied to the top of the implanted electrode, along the longitudinal direction (figure 1). In practice, the load is not applied in the longitudinal direction because the electrode is fixed to the skull. To facilitate comparison of results with Lee et al. (2005), it is assumed that the electrode moves longitudinally and the brain is fixed. Motion in other directions are not considered in this analysis because the longitudinal micromotion direction is dominant (Lee et al., 2005).

Brain micromotion is a continuous process that can arise from physiological, behavioral, and mechanical sources such as respiration and cardiac rhythm,

spontaneous head movements, and disturbances of the implant, respectively (Reichert, 2008). This micromotion can then be translated into mechanical stresses and strains in the brain region neighboring the electrode, which may lead to compression, expansion, and tearing of the neural tissue (Reichert, 2008). For simplicity, convenience in modeling, and comparison of our micromotion results with published literature, an inverse load application was considered (Lee et al., 2005; Zhu et al., 2011). Micromotion for the FZ-Si, HV-Si, and LE-Si finite element model was simulated by imposing a 1 μN force (pressure = 0.002168 μN/μm^2) to the top of the silicon electrode. The load was applied along the longitudinal direction (negative "Y" direction), which is the dominant micromotion direction of the brain (Lee et al., 2005). Lee et al. (2005) applied a load of 1 μN force (pressure = 0.002168 μN/μm^2) to achieve physiologically realistic displacements attributed to micromotion for LE-Si. To facilitate comparison with the study by Lee et al. (2005), this paper will highlight results that considers a 1 μN force application. For hydrogel-coated electrodes, realistic displacements and strain contour fields were achieved when a constant pressure of 0.002168 μN/μm^2 (1 μN force) was applied to the top surface of only the silicon portion of the neural electrode.

3. Results

3.1. Finite Element Model Validation

The fractional Zener (FZ) constitutive model was used to simulate unconfined compression experiments performed by Bentil (2013) for verification of the UMAT code. Taking advantage of symmetry, a 2D axisymmetric FE model captured the cylindrical geometry of the brain tissue sample and impermeable platen. The dimensions of the brain tissue samples were similar to those used in the experiments by Bentil (2013). The purpose of this initial FE study was to ensure that the physical experiment was modeled accurately using the UMAT code for the fractional Zener constitutive model. FE model validation was performed by comparing the resulting displacements and forces (or strains

and stress) with that obtained experimentally. The FE results agreed with the experimental data.

Lee et al. (2005) performed finite element simulations using the software ANSYS Version 7.1 to analyze the strain fields due to simulated micromotion of a single Michigan silicon-substrate microelectrode shank (LE-Si case). The same simulations were performed using the software ABAQUS (ABAQUS, 2011) for validation of the method. The von Mises strain and electrode displacement results from our analysis were in agreement with the work by Lee et al. (2005). Lee et al. (2005) represented the effective shear strain (ε_e) on the surfaces of the symmetry planes of the brain tissue by using the von Mises strain described by equation (2).

$$\varepsilon_e = \frac{1}{1+\nu}\sqrt{\frac{1}{2}\left[(\varepsilon_1-\varepsilon_2)^2+(\varepsilon_2-\varepsilon_3)^2+(\varepsilon_3-\varepsilon_1)^2\right]}, \tag{2}$$

where ν is Poisson's ratio and the Principal strains are described by ε_1, ε_2, and ε_3. The software ABAQUS contains a built-in output variable called "maximum principal logarithmic strain", which gives nearly identical results to what was presented as von Mises strain in Lee et al. (2005). Because of the close agreement, all strain contour plot results in what follows will use the maximum principal logarithmic strain. The logarithmic strain in the contour plot legend is denoted by "LE" and should not be confused with the abbreviation for linear elastic.

3.2. Maximum Principal Logarithmic Strain

The maximum principal logarithmic strain for the silicon-substrate electrode was negligible, due to the large Young's modulus value for the silicon material. This was not the case for the soft brain tissue and hydrogel coating. Therefore the maximum principal logarithmic strain results will focus on the brain and hydrogel coating, but not the silicon-substrate electrode.

Histograms were generated using the maximum principal logarithmic strain to gain insight into the effect of electrode coating thickness and material choice

on reducing the resulting strain caused by micromotion. The percentage of elements was used to generate the strain histograms, but the elements in the brain or electrode coating were of different sizes due to mesh refinement near the electrode tip. Strain histograms using a volume percentage were considered to assess whether the histograms plotted using the percentage of elements may be skewed or yield a different trend. A comparison of strain histograms by percentage of element and percentage of volume shows that the trend will be similar, since the same mesh was used for all simulations. However, the plot with the percentage of elements exaggerates the strain closer to the electrode tip, due to the mesh refinement performed in this region (figure 2). For illustrative purposes, all future strain histogram plots will only consider percentage of elements. To gain a better perspective of the strain in the brain and electrode coating, both strain histograms and strain contour plots will be used to illustrate the brain-electrode FE results.

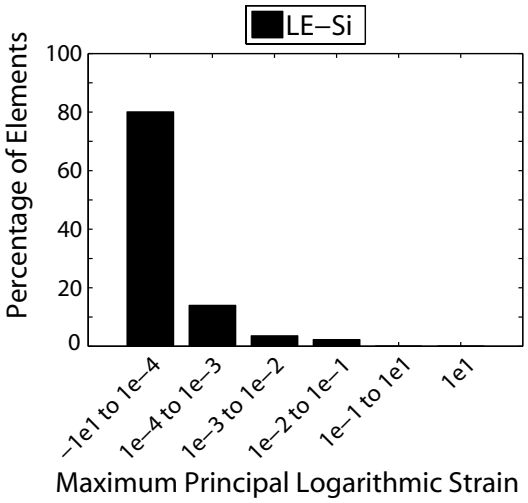

(a)

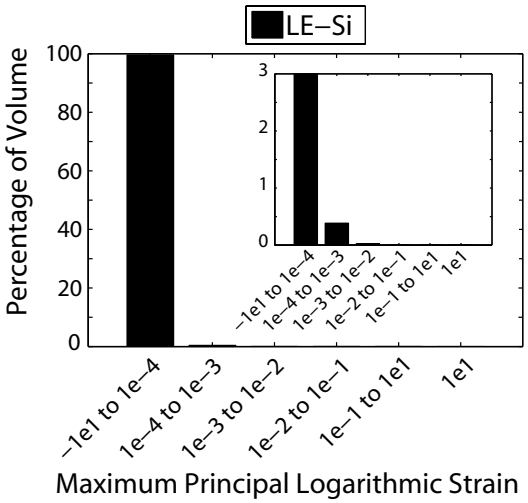

(b)

Figure 2: Maximum principal strain histogram comparison for the brain using LE-Si (constants from Lee et al. (2005)) for (a) Percentage of Elements vs. (b) Percentage of Volume. The insert in (b) is enlarged to show the values in the volume range from 0 to 3 percent.

3.3. Stress-Strain Curve

A FE analysis was performed to study the mechanical behavior of a cylindrical sample of brain tissue, when the top surface is subjected to a 5 mm/min compressive rate and the tissue is described using the FZ, HV, or LE constitutive model. Lagrange stress versus true strain curves were then generated to capture the mechanical response. The Lagrange stress (or engineering stress) is obtained by dividing the vertical force on the tissue's top surface by the initial cross-sectional area of the specimen. True strain (ε) is defined by equation (3).

$$\varepsilon = \ln \lambda, \tag{3}$$

where λ is the stretch in the vertical direction.

A plot of Lagrange stress versus true strain for the three material models considered is illustrated in figure 3. The range of stresses for strains below 30% in figure 3 can be achieved experimentally (Miller and Chinzei, 1997; Miller, 1999). The LE stress-strain curves depicted by figure 3 were generated using both (i) constants provided by Lee et al. (2005) and (ii) constants obtained by fitting the LE constitutive model to the *in vitro* pig brain unconfined experimental data of Bentil (2013). The fitted constants for Bentil (2013) correspond to brain tissue that were tested less than 6 hours *post mortem*.

Following optimization of the coefficients using Bentil (2013) experimental data, the nearly incompressible brain yielded a Young's modulus of 1696 Pa and a Poisson's ratio of 0.49. This Young's modulus value was approximately 9 times softer than the coefficient used by Lee et al. (2005). For strains in the brain less than 5%, the stress-strain curves of figure 3(c) show that the LE constants by Bentil (2013) had a similar behavior to the FZ and HV material model and the range of stresses (0 - 100 Pa) is representative of brains subjected to low strain, unconfined compression experiments (Miller and Chinzei, 1997; Miller, 1999; Bentil, 2013).

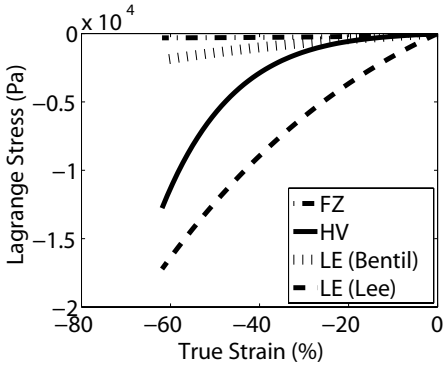

(a)

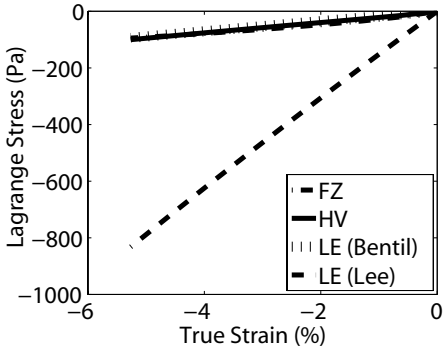

(b)

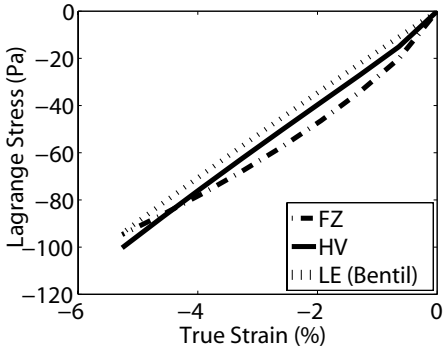

(c)

Figure 3: Stress-strain curves for the brain using FZ, HV, and LE constitutive models. (a) Large strains and (b) Small strains. (c) Enlarged to show detail. Negative values imply compression. LE material properties were from Lee et al. (2005) and based on experimental data by Bentil (2013).

The loads applied to the top surface of the neural electrode FE simulations yielded strains in the brain tissue that were less than 5%. According to figure 3(b) or figure 3(c), such small strains imply that the simulation results using the constitutive models described as FZ, HV, and LE (using constants based on the experimental work by Bentil (2013)) for the brain and/or hydrogel coating should be nearly identical. This was found to be the case across the varying coating thickness and adhesive behaviors. Figures 4 and 5 shows strain contour plots for FZ-SiFZ, HV-SiHV, and LE-SiLE (using brain constants by both Bentil (2013) and Lee et al. (2005)) given a 5 μm and 80 μm hydrogel coating thickness, respectively. Adhesive behavior ranging from frictionless to bonded are also illustrated in both figures 4 and 5. When a frictionless or a friction coefficient of 0.5 or 1.0 was considered, the shape of the strain distribution in the contour plots was similar for a given brain-electrode aggregate. Furthermore, the largest strains were located in the hydrogel coating closest to the silicon electrode tip. Strains ranging from 1×10^{-2} to 1×10^{1} were present around the electrode tip and lower strains were obtained radially outward from the tip. For the bonded case, the distribution of strain was along the length of the electrode. The maximum principal logarithmic strain was in the 1×10^{-4} to 1×10^{-3} range. For cases where the brain or coating was described as FZ, HV, and LE (via Bentil (2013) constants), higher strains between 1×10^{-3} to 1×10^{-2} were also present along parts of the electrode shank due to the softer material description for the brain tissue. The histograms in figures 6 and 7 correspond to the contour plots for FZ-SiFZ described in figures 4 and 5. Figures 6 and 7 represent data for the brain and hydrogel coating, respectively. In these histograms, a decrease in the spread of strain due to increased adhesive behavior is depicted. The strain ranges are skewed toward smaller values with increased adhesive behavior. This trend was also present for HV-SiHV and LE-SiLE (using constants for both Bentil (2013) and Lee et al. (2005)) and varying material description combinations of the brain-electrode aggregate (e.g. FZ-SiHV and HV-SiLE).

Strains for the brain or hydrogel coating described using linear elastic con-

stants by Lee et al. (2005) were lower when compared with simulations using the elastic modulus of the brain based on Bentil (2013) data. This was attributed to the stiffer description of the tissue using constants by Lee et al. (2005). Table 4 shows the average percent difference of maximum principal logarithmic strain for LE-SiLE using the data presented in figures 4 and 5. The percent difference was averaged across the four different adhesive conditions considered. An increase in electrode coating thickness resulted in an increase of the percent difference using the maximum value of the maximum principal logarithmic strain.

Table 4: Percent difference of the maximum value of the maximum principal logarithmic strain for LE-SiLE brain-electrode aggregate with a 5 μm and 80 μm coating thickness.

	Coating Thickness	Percent Difference (%)	
		Brain	Coating
LE-SiLE*	5 μm	128 $\pm$ 33	133 $\pm$ 16
	80 μm	155 $\pm$ 5	154 $\pm$ 3

* LE material constants provided by both Lee et al. (2005) and Bentil (2013) were used for the percent difference calculation.

Comparable results for the maximum principal logarithmic strain histograms and contours were obtained when the brain and hydrogel coating were described using FZ, HV, and LE (via Bentil (2013) constants). To streamline the presentation of results, in what follows, this paper will only highlight cases using the FZ-model and not include the same result for HV or LE (via Bentil (2013) constants), to eliminate redundancy. Unless otherwise mentioned, the LE constitutive model results will be described using the constants provided by Lee et al. (2005).

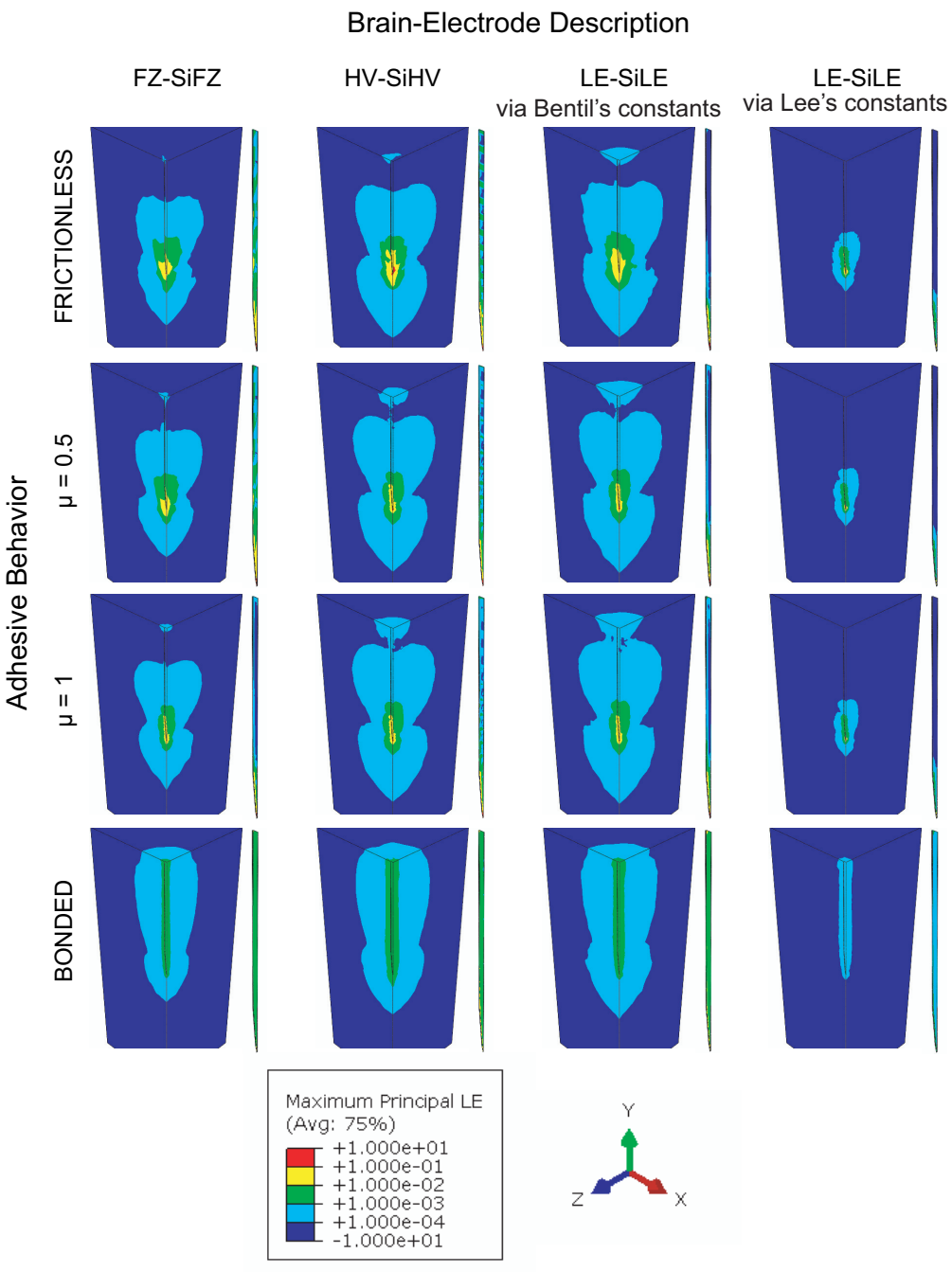

Figure 4: Maximum principal logarithmic strain contour plots for both the brain and electrode coating with a coating thickness of 5 μm. Each column corresponds to a brain-electrode aggregate described as FZ-SiFZ, HV-SiHV, or LE-SiLE. The adhesive behavior varies by row.

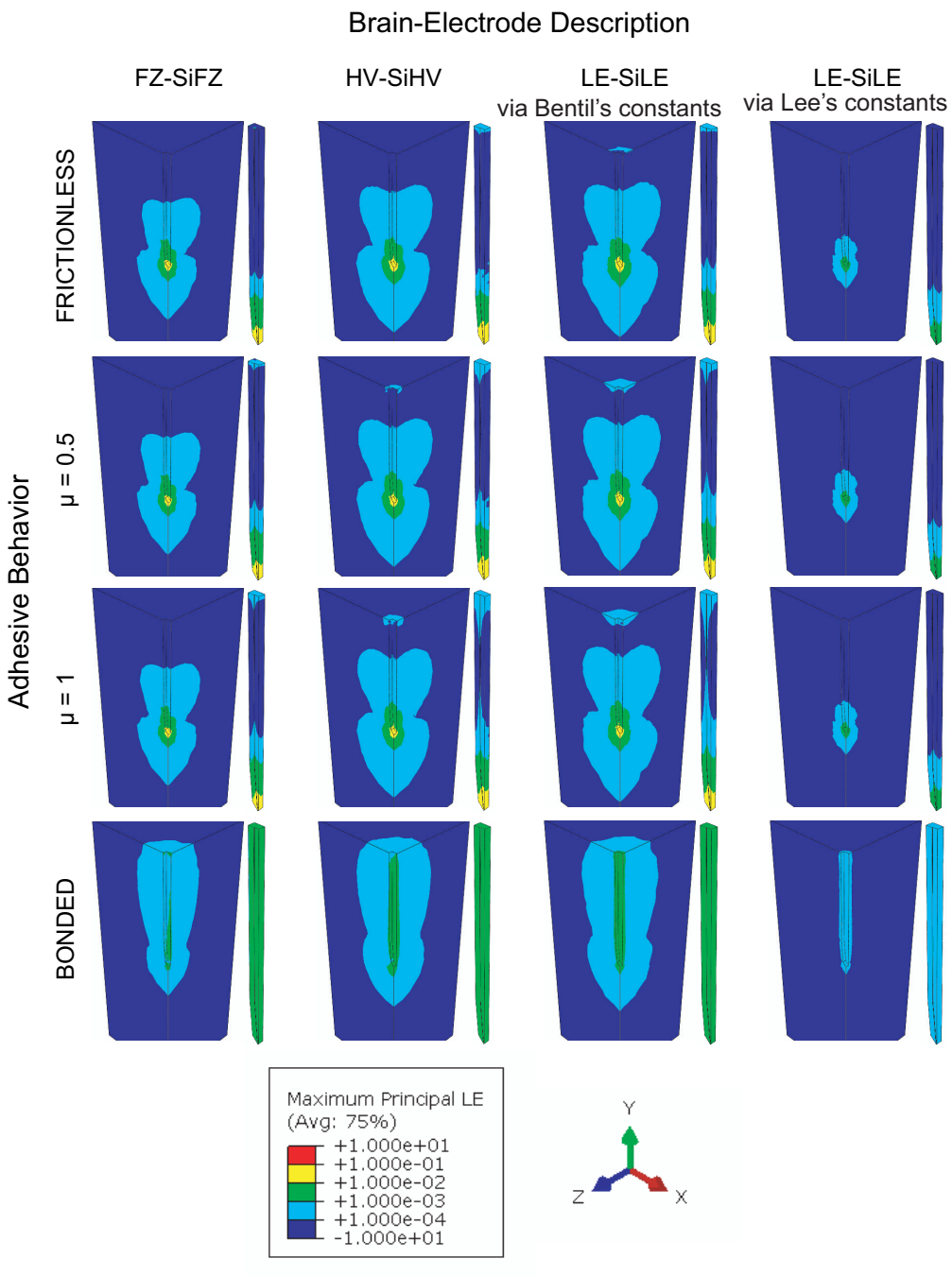

Figure 5: Maximum principal logarithmic strain contour plots for both the brain and electrode coating with a coating thickness of 80 μm. Each column corresponds to a brain-electrode aggregate described as FZ-SiFZ, HV-SiHV, or LE-SiLE. The adhesive behavior varies by row.

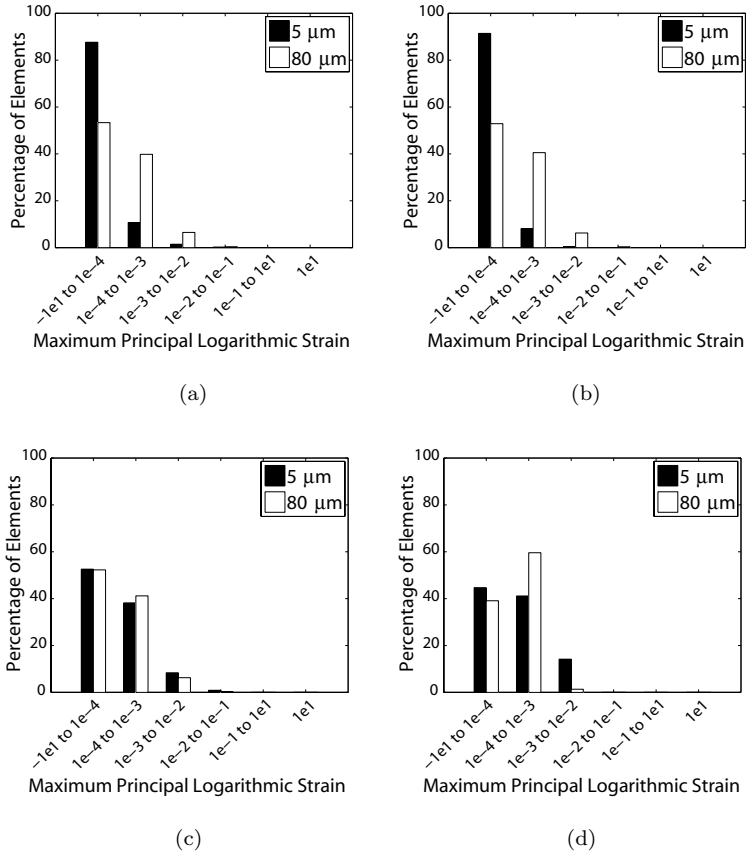

Figure 6: Maximum principal logarithmic strain histograms of the brain for FZ-SiFZ. A comparison between 5 μm and 80 μm hydrogel coating thickness is made for the adhesive behavior described as (a) frictionless, (b) $\mu = 0.5$, (c) $\mu = 1$, and (d) bonded.

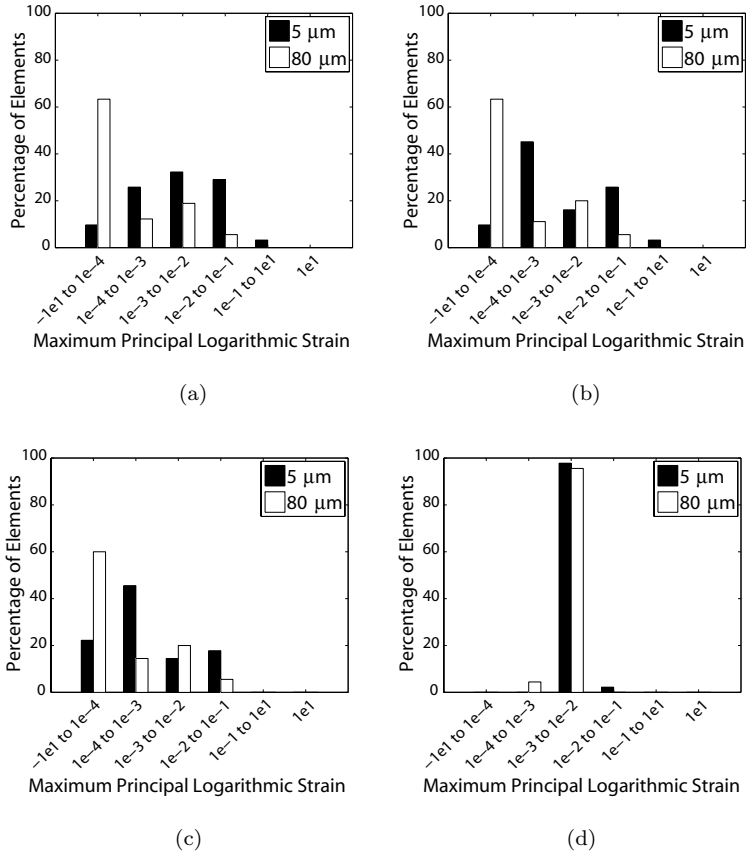

Figure 7: Maximum principal logarithmic strain histograms of the electrode coating for FZ-SiFZ. A comparison between 5 μm and 80 μm hydrogel coating thickness is made for the adhesive behavior described as (a) frictionless, (b) $\mu = 0.5$, (c) $\mu = 1$, and (d) bonded.

3.4. Hydrogel-coated Electrode

As the electrode coating thickness increases from 5 μm to 80 μm, the percentage of elements in the higher maximum principal strain range decreases and the percentage in the lower maximum principal strain range increases for the brain (figure 6) and electrode coating (figure 7). This general trend was present in simulations where the brain-electrode material description and adhesive behavior was held constant. This result suggests that coating the silicon electrode reduces the strains present in the brain tissue. The higher strains that the brain

would typically sustain are transferred to the hydrogel coating.

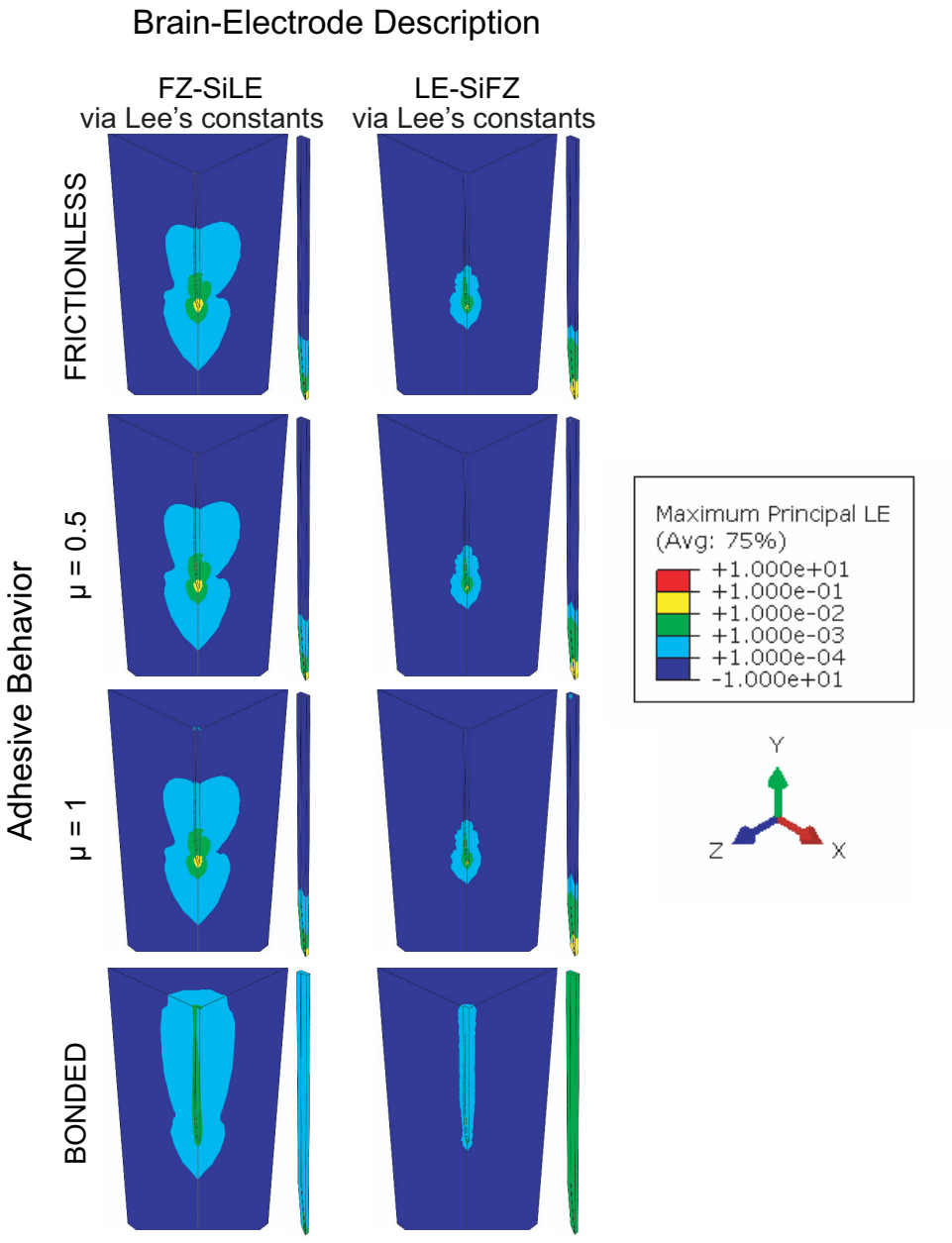

Figure 8: Maximum principal logarithmic strain contour plots for both the brain and electrode coating with a coating thickness of 40 μm. Each column corresponds to a brain-electrode aggregate described as either FZ-SiLE or LE-SiFZ. The adhesive behavior varies by row.

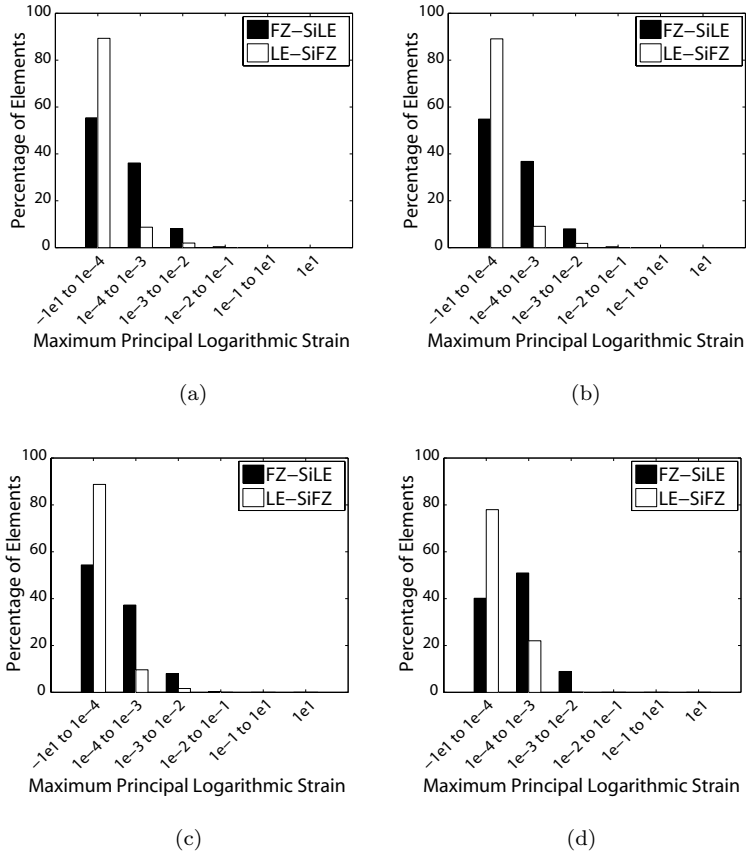

Figure 9: Maximum principal logarithmic strain histograms of the brain for FZ-SiLE and LE-SiFZ. Lee et al. (2005) constants were used to describe the linear material and the hydrogel coating thickness was 40 μm. The adhesive behavior is described as (a) frictionless, (b) $\mu = 0.5$, (c) $\mu = 1$, and (d) bonded.

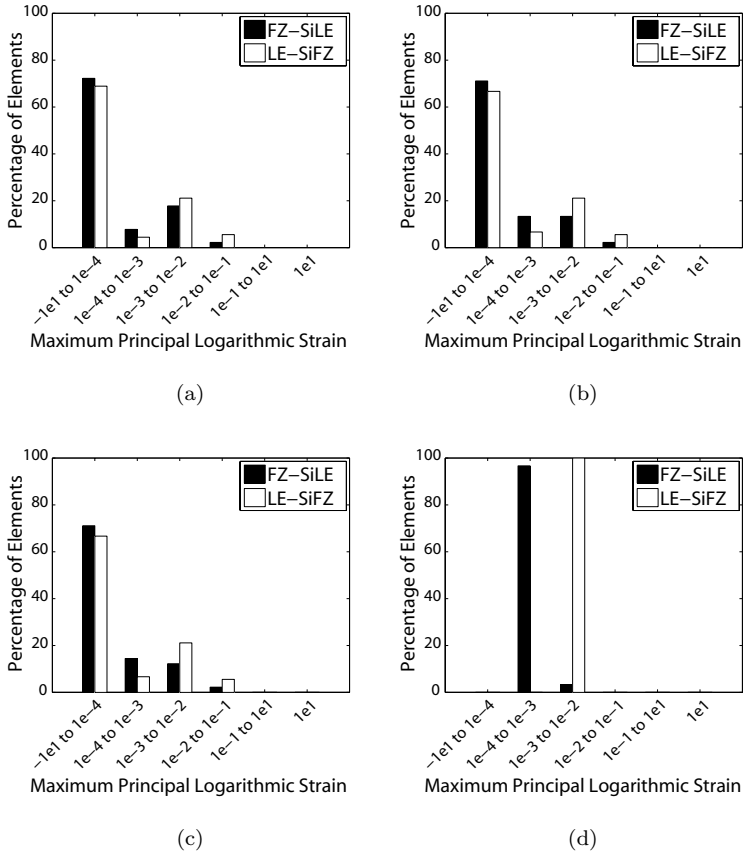

Figure 10: Maximum principal logarithmic strain histograms of the electrode coating for FZ-SiLE and LE-SiFZ. Lee et al. (2005) constants were used to describe the linear material and the hydrogel coating thickness was 40 μm. The adhesive behavior is described as (a) frictionless, (b) $\mu = 0.5$, (c) $\mu = 1$, and (d) bonded.

When the brain-electrode material description and the electrode coating thickness were held constant, but the adhesive behavior was allowed to vary, there was minimal difference in the maximum principal strain for the following adhesive conditions: frictionless, $\mu = 0.5$, and $\mu = 1$. There was a difference in the maximum principal strain when a bonded adhesive condition was specified. An example of this difference is illustrated by the strain contours of FZ-SiLE and LE-SiFZ when a 40 μm coating thickness is considered (figure 8). Figures 9 and 10 are the histograms of figure 8 for the brain and electrode coating, respec-

tively. The strain histograms for the brain tissue and electrode coating model were always shifted to lower strain values and the spread of strain decreased for the bonded case. Figure 11 uses the FZ-SiFZ brain-electrode description as an example to illustrate that the strain contours are different between the bonded case and non-bonded cases, with the bonded case showing strains more uniformly distributed along the length of the electrode, regardless of the coating thickness. As the thickness increases and the adhesive behavior approaches the bonded case, the percentage of elements with higher strain values decreases. This trend occurs for all brain-electrode material model combinations.

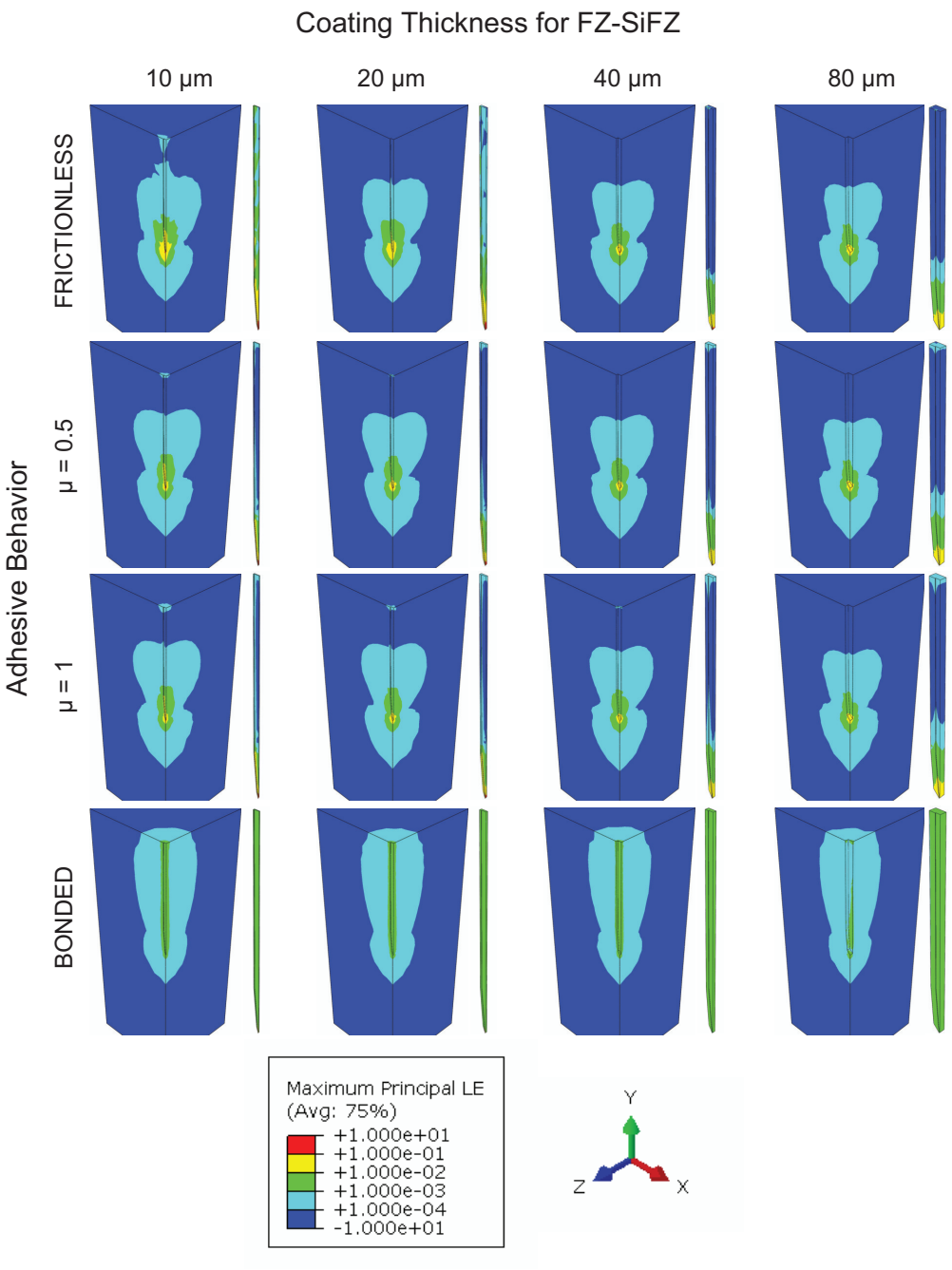

Figure 11: Maximum principal logarithmic strain contour plots of FZ-SiFZ for both the brain and electrode coating. The coating thicknesses range from 0 μm (uncoated) to 80 μm. The adhesive behavior varies by row.

Figures 8, 9, and 10 also highlight the influence of a soft material description for brain given a stiff hydrogel coating (FZ-SiLE) and stiff brain tissue due to a soft hydrogel coating (LE-SiFZ). As expected, the strain magnitudes in the brain and coating were higher when a softer material description was considered. Figure 8 suggests that the soft viscoelastic brain "senses" the stiffer linear elastic hydrogel coating. This mechanical mismatch may explain the reason why the strain contour distribution is not shifted toward the lower strain levels. Across all adhesive conditions, the distribution of strain in the contour plots was smaller when a stiffer material description was applied for either the brain or hydrogel coating.

3.5. Maximum Electrode Displacement

The maximum electrode displacement was considered as a metric to quantify the effect of coating thickness and adhesive behavior on micromotion. These electrode displacement values can potentially be used to validate whether the FE simulation results yield physiologically realistic micromotion given the chosen material model for capturing the behavior of the brain tissue. Lower displacements suggest an improvement in micromotion reduction.

Electrode displacements when the FZ, HV, or LE (via Bentil (2013) constants) material descriptions were used for the brain or coating were similar in magnitude, due to the simulations being conducted at small strains. Figure 12 illustrates this behavior by considering LE-SiLE (using Bentil (2013) constants) and HV-SiFZ for a 20 μm hydrogel coating thickness. The adhesive behavior was allowed to vary. The percent difference for the displacement of the electrode in brain-electrode aggregates using FZ, HV, or LE (via Bentil (2013) constants) for a given adhesive condition did not exceed 20%. As friction increases, the total displacement of both coated and uncoated electrodes decrease due to increased simulated adhesion with the brain tissue. This trend was present for all electrode coating thicknesses. The displacement of the bonded brain to the electrode was always less than 2 μm. When the adhesive behavior was held constant, while the electrode coating thickness increased, there was a decrease

in electrode displacement (figure 13). Modeling the hydrogel coating using the linear elastic material constants provided by Lee et al. (2005) always yielded smaller electrode displacements (figure 13) when compared with coating described using FZ, HV, or LE (via Bentil (2013) constants). Examination of the stress-strain curve (figure 3) confirmed that the magnitude of stress and strain for the LE material (via Lee et al. (2005) constants) was always larger when considering strains even as high as 60%, due to the stiffer response from the large Young's modulus. This suggests that the linear elastic constants for the brain provided by Lee et al. (2005) will yield underestimated finite element results for both the strain and displacement, even when small strains are considered.

Electrodes without any hydrogel coating experienced the largest and smallest displacement. The largest displacement value occurred when a frictionless adhesive behavior was considered and the magnitude depends on the constitutive model considered for the brain. The smallest electrode displacement was obtained when the bonded adhesive condition was applied.

Given a 1 μN force, the maximum electrode displacement for LE-Si (using elastic constants from Lee et al. (2005) and LE-Si (using Bentil (2013) constants) with a frictionless adhesive condition was 16.5 μm and 42.4 μm, respectively. A comparative study for LE-Si (using Bentil (2013) elastic constants for the brain) showed that a pressure of 0.00089 $\mu\text{N}/\mu\text{m}^2$ (0.41 μN force) was necessary to yield a 16.5 μm electrode displacement for the frictionless adhesive behavior. This displacement was physiologically realistic since it did not exceed 25 μm (Lee et al., 2005). A lower force was needed to achieve the same electrode displacement as Lee et al. (2005) due to the softer material description for the brain tissue using the linear elastic material constants from Bentil (2013) data.

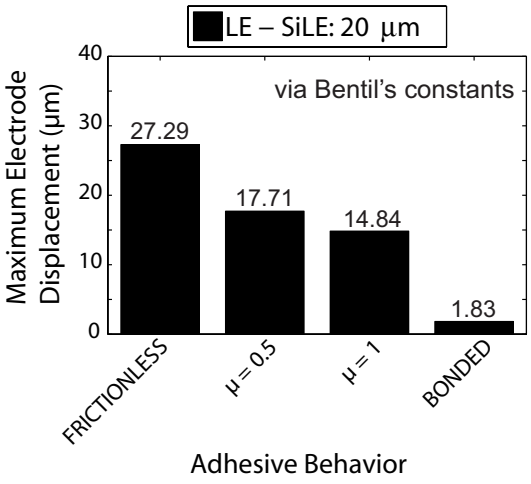

(a)

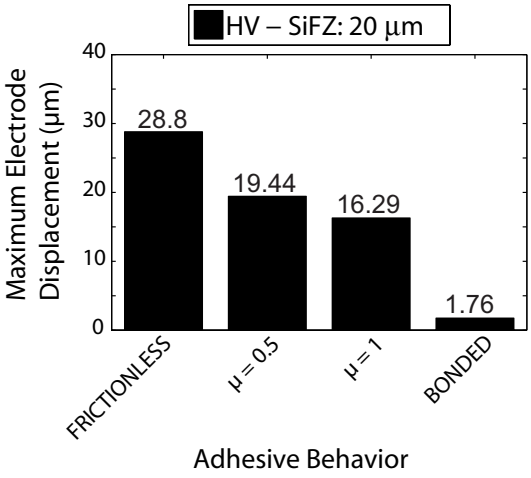

(b)

Figure 12: Electrode displacement decreases with increased adhesion, regardless of coating status. 20 μm hydrogel coating thickness for the electrode using (a) LE-SiLE via constants from Bentil (2013) and (b) HV-SiFZ condition.

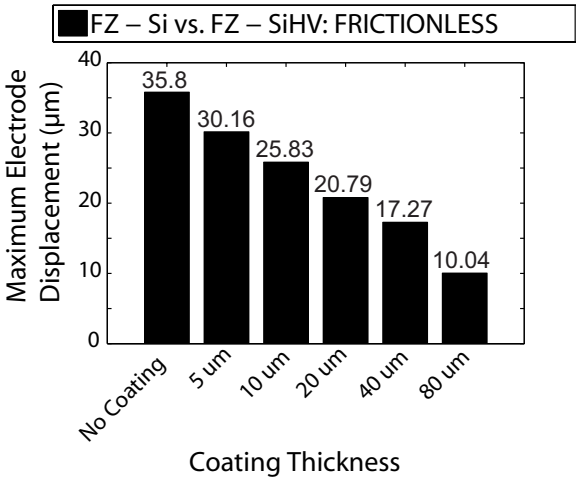

(a)

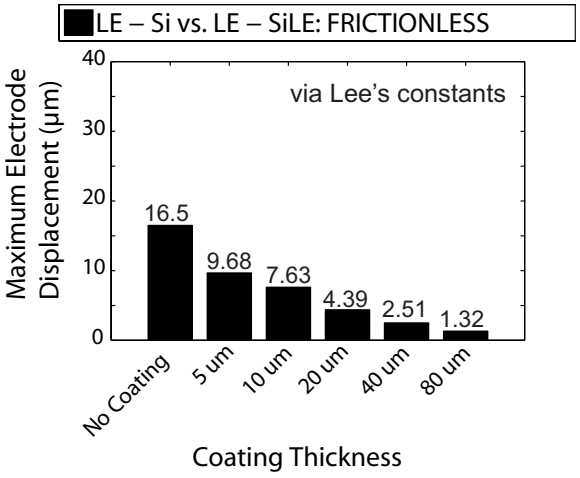

(b)

Figure 13: Electrode displacement decreases with increased coating thickness, regardless of coating status. (a) Uncoated case using FZ-Si and HV coating (FZ-SiHV) and (b) Uncoated case using LE-Si and LE coating (LE-SiLE) via constants from Lee et al. (2005).

3.6. Effect of Variable Linear Elastic Stiffness Properties

The optimal hydrogel coating stiffness, from a design perspective, was examined by conducting simulations using the LE-SiLE brain-electrode aggregate.

The LE brain in this model utilized material constants by Bentil (2013), for simplification purposes. The Young's modulus for the LE coating was varied to study the incongruent stiffness constants between the brain and hydrogel coating. Since the FE simulations considered small strains (figure 3(c)), the results would be interchangeable with cases where the viscoelastic FZ or HV material model was used to describe the brain and hydrogel coating.

The effect of variable coating stiffness was analyzed using finite elements by considering a frictionless adhesive behavior and a 40 μm hydrogel coating thickness for LE-SiLE brain-electrode aggregate. The stiffness of the brain and hydrogel coating were described using the Young's modulus from the LE material model. The hydrogel coating stiffness ranged from 1696 Pa to 100 kPa, but the brain stiffness was held constant at 1696 Pa. The top of the implanted electrode was subjected to a 16.5 μm displacement along the longitudinal direction to examine the effect of coating stiffness. A study by Lee et al. (2005) showed that a 16.5 μm displacement was within the range of physiological micromotion for the brain due to respiration. For comparative purposes, a 16.5 μm displacement was considered for the LE-SiLE brain-electrode aggregate.

As the hydrogel coating stiffness increased from 1696 Pa to 100 kPa, the maximum principal logarithmic strain increased nonlinearly for the brain (figure 14(a)) and decreased nonlinearly for the hydrogel coating (figure 14(b)). Increasing the coating stiffness (i.e. 1696 Pa) by a factor of 50 increased the strain in the brain by 23% and caused a 90% strain reduction for the electrode coating. Figure 14 captures this behavior using the maximum value for the maximum principal logarithmic strain. A stiffer material description for the hydrogel coating did not improve biocompatibility but rather introduced strains that were transferred to the brain tissue. However, stiffer electrode coatings are still an improvement over the uncoated silicon-substrate (e.g. LE-Si) as evidenced by lower strain magnitudes. The maximum value for the maximum principal logarithmic strain in the brain when LE-Si (using Bentil (2013) constants) subjected to a 16.5 μm displacement was 0.14. As the coating stiffness increases (figure 14(a)), the maximum value for the maximum principal log-

arithmic strain is lower than the uncoated case, but is approaching the 0.14 value. When the hydrogel coating becomes much stiffer than the brain (less than 3 times stiffer or greater than 30 times stiffer), there is a relatively small change in the maximum strain for both the brain and hydrogel coating. This suggests that there is a critical hydrogel stiffness beyond which the coating will no longer effectively reduce the strain in the brain. The results indicate that the optimal strain reduction occurs when the modulus for both the brain and the hydrogel coating are comparable.

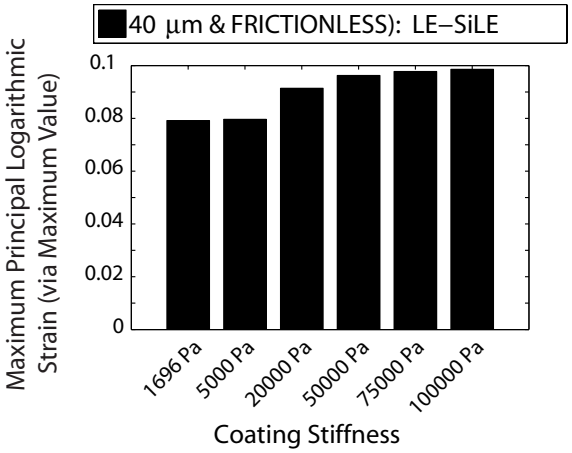

(a)

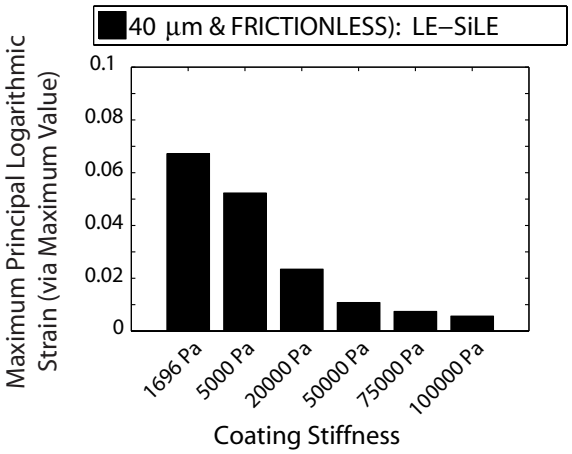

(b)

Figure 14: Varying the hydrogel coating stiffness (via Young's modulus) for LE-SiLE with a frictionless adhesive behavior and a 40 μm hydrogel coating thickness. Maximum value of the maximum principal logarithmic strain for (a) brain and (b) hydrogel coating.

3.7. Effect of Variable Load Applications

A study that considers different load applications was conducted to determine which interpretation is able to capture the strain distribution changes in the brain tissue attributed to varying hydrogel coating stiffness properties. For

this study, the material model, adhesive behavior, and hydrogel coating thickness were held constant. Examples of the load application scenarios for the electrode that were considered for identification of the optimal hydrogel coating stiffness for improved biocompatibility included: (i) the specification of a constant electrode displacement into the brain tissue and (ii) application of a constant pressure on the top of the electrode. The results showed that FE simulations where displacement boundary conditions were applied are ideal as strain changes attributed to varying hydrogel coating stiffness follow a realistic trend (i.e. improved biocompatibility with softer hydrogel coating). Application of a constant pressure or force to the silicon portion of the electrode shank caused the maximum longitudinal displacement of the electrode and maximum principal logarithmic strain for the brain and hydrogel coating to decrease with increased coating stiffness. This result does not realistically capture the trend of strain in the brain tissue due to variable hydrogel coating stiffness. However, it does describe the response of the electrode coating when the stiffness is varied.

A stress-strain curve for three linear elastic materials with different Young's moduli can be used to explain why application of a constant pressure yields a counter-intuitive result. Consider the stress-strain curves in figure 15, which features three hypothetical materials. The Young's moduli for the three materials in ascending order are E_1, E_2, and E_3.

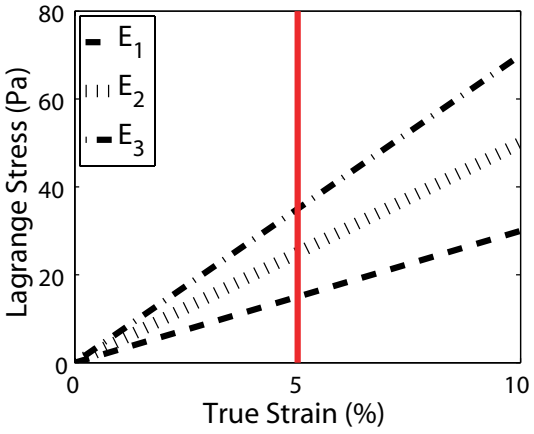

(a)

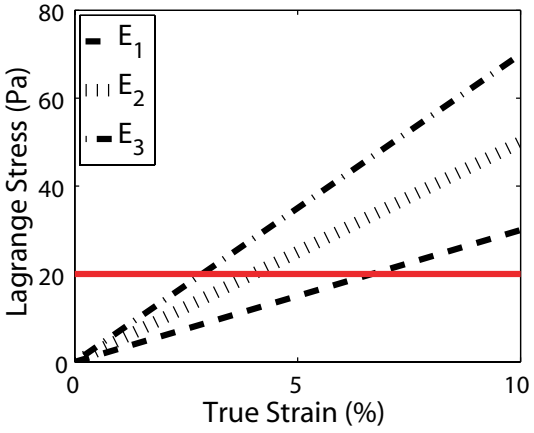

(b)

Figure 15: Stress-strain curve of three hypothetical linear elastic materials. Considering (a) constant displacement (strain) and (b) constant force (stress). Line in red indicates section considered.

For the constant electrode displacement case, consider taking a vertical section from the stress-strain curve (figure 15(a)). Considering the intersection points between the three stress-strain curves and the red section line, it is observed that a smaller modulus yields a lower stress at a prescribed strain (or displacement) value. This could be interpreted as an improvement in biocom-

patibility due to a soft material description for the hydrogel coating. A constant pressure (or force) application on the electrode is akin to taking a horizontal section across the stress-strain curve (figure 15(b)). As the modulus of the material decreases, larger strains will be experienced for a given applied load, or stress. Since we are using strain (stress) reduction to assess biocompatibility, a correlation that shows softer coating leads to larger strains implies a counter-intuitive reduction in biocompatibility, but this is really an artifact created by the choice to hold force (or pressure) constant.

3.8. Optimization Study to Identify Parameters for Improved Coated-Electrode Design

An optimization study was conducted on the simulation data (full factorial design) using the software JMP (JMP, 2015) to identify the optimal thickness as a function of coating material and adhesive behavior that will result in the smallest maximum strain in the brain tissue. First, a standard least squares regression was applied to a linear fixed effect model. The R-Square value, which is a statistical measure quantifying the fit of the data with the regression line, was used to select the best fit model. The best fit model with maximum strain as the response (dependent variable) consisted of the following factors (independent variables): coating material, adhesive behavior, coating thickness, and all possible interactions (binary and tertiary). The R-Square value from the regression analysis of FZ, HZ, and LE (Bentil, 2013) descriptions for the coating and/or brain was 0.76. A R-Square value of 0.81 was calculated from the regression analysis of FZ, HZ, and LE (Lee et al., 2005) descriptions for the coating and/or brain. Figure 16 is a cube plot that illustrates the maximum strain values as a function of the coating material, adhesive behavior, and thickness from the statistical analysis where the linear elastic constants were described by Bentil (2013) or Lee et al. (2005). The smallest maximum strain in the brain tissue using FZ, HV, and linear elastic constants described by Bentil (2013) was 0.0058 and occurred when an 80 μm coating thickness and a FZ description for both the brain and hydrogel coating on the silicon electrode was considered

(figure 16a). The largest maximum strain (0.1973) in the brain tissue occurred for a 5 μm coating thickness with a LE description for the brain and hydrogel-coated silicon electrode. When considering FZ, HV, and linear elastic constants described by Lee et al. (2005), the smallest maximum strain in the brain tissue was 0.0058 and occurred when an 80 μm coating thickness and a FZ description for both the brain and hydrogel coating on the silicon electrode was considered (figure 16b). The largest maximum strain in the brain tissue was 0.1718 and occurred for a 5 μm coating thickness with a HV description for the brain and LE (Lee et al., 2005) hydrogel-coated silicon electrode. LE-SiLE did not yield the maximum condition due to the increased mechanical mismatch between the soft brain (HV) and rigid electrode with stiffer coating description using LE properties provided by Lee et al. (2005). For both linear elastic descriptions, the bonded adhesive condition yielded the minimum value for maximum principal logarithmic strain in the brain. The optimization study confirmed that as coating thickness increases, the maximum logarithmic strain in the brain tissue will decrease.

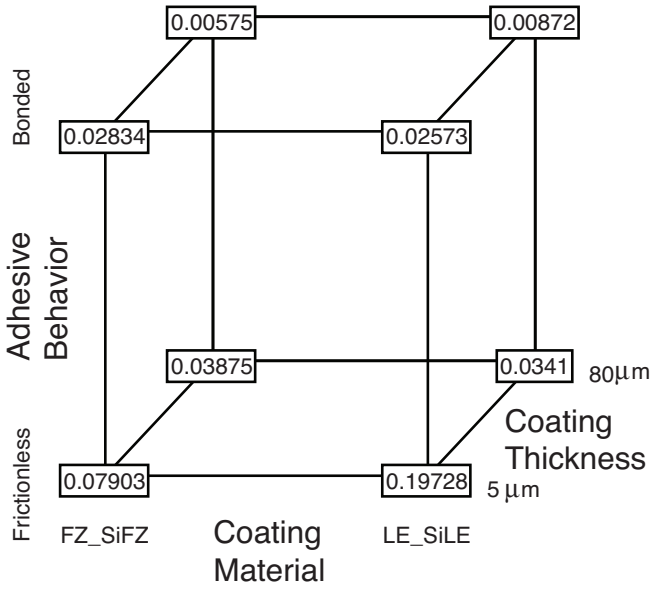

(a)

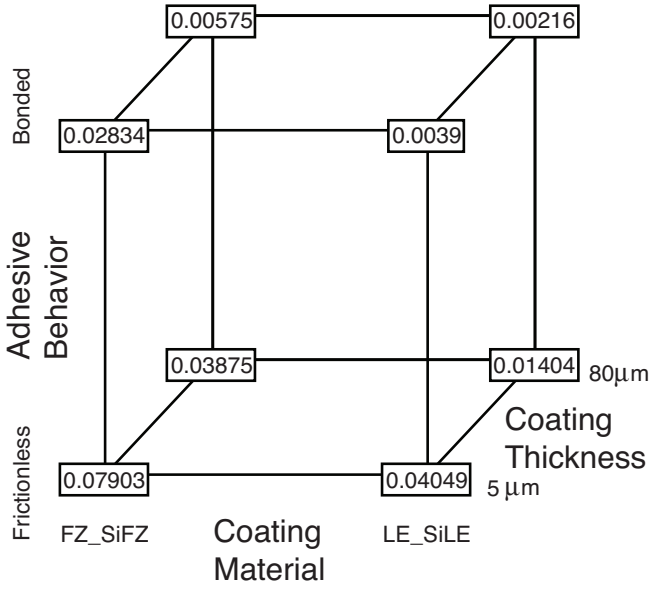

(b)

Figure 16: Cube plot of maximum principal logarithmic strain in the brain as a function of coating material, adhesive behavior, and coating thickness using linear elastic constants optimized by (a) Bentil (2013) and (b) Lee et al. (2005).

An analysis of variance (ANOVA) was used to identify the parameters that will guide and influence the design of coated electrodes. The significance level for this statistical analysis was 0.05. Parameters that yielded p-values less than 0.05 were considered to be significant and will influence the strain response in the brain. Table 3.7 summarizes the significant and non-significant parameters for the best fit linear fixed effects model. The tertiary interaction between the coating material, adhesive behavior, and coating thickness are higher order factors which were not significant, but may be used to describe random variations in the maximum principal logarithmic strain.

Table 5: Parameters influencing coated-electrode design using maximum principal logarithmic strain as a metric for micromotion to assess biocompatibility improvement. The significance level for the linear fixed effects model was 0.05. Parameters with values less than 0.05 will significantly effect the maximum principal logarithmic strain value in the brain.

		Maximum Principal Logarithmic Strain	
Linear Fixed Effects Model Parameters	Interaction	†LE	††LE
Coating Material		<0.0001	<0.0001
Adhesive Behavior		<0.0001	<0.0001
Coating Thickness		<0.0001	<0.0001
Coating Thickness * Adhesive Behavior	binary	<0.0001	<0.0001
Coating Thickness * Coating Material	binary	0.0045	0.0059
Coating Material * Adhesive Behavior	binary	0.0097	<0.0001
Coating Material * Adhesive Behavior * Coating Thickness	tertiary	0.3798	0.0561

† LE material constants provided by Bentil (2013) was used in the regression analysis.

†† LE material constants provided by Lee et al. (2005) was used in the regression analysis.

4. Discussion and Conclusion

Polymer-based and silicon implantable electrodes with two- and three-dimensional

surfaces, electrodes on flexible mesh substrates, and free-floating and untethered wireless electrodes are examples of neural prosthetic designs available for recording and stimulation in the central or peripheral nervous system (Maharbiz et al., 2017; Cutrone et al., 2015; Xiang et al., 2016). Three-dimensional neural probes are advantageous when compared to the two-dimensional counterpart since they facilitate recording and stimulation at various layers within the cortex. Electrodes on flexible mesh substrates enable electronic components (e.g. wireless transmitters) to be integrated onto the substrate and conform to the curvature of the brain (Xiang et al., 2016). Free-floating and untethered electrodes are conducive for wireless continual transmission of signals using electromagnetic backscattering (Maharbiz et al., 2017). Given the various electrode designs available, our results only apply to implantable silicon-based electrodes. Our work has shown that hydrogel-coated neural microelectrodes improve the biocompatibility of implanted silicon electrodes and is a viable solution to reduce micromotion and scar tissue encapsulation associated with the use of these electrodes (Kim et al., 2010; Schendzielorz et al., 2014). Coating electrodes that are fabricated with biocompatible materials is not necessary if the mechanical properties of the electrode is comparable with neural tissue (Jorfi et al., 2015). The use of biocompatible coatings result in a reduction in the mechanical mismatch between the brain and rigid electrode, and therefore a reduction in the inflammatory response that would lead to microelectrode encapsulation by glia cells (Sridharan et al., 2013). However, biocompatible hydrogel coatings can swell in time and produce an inflammatory response in the brain. Although our study did not consider swelling of the hydrogel coating, swelling is expected to decrease with decreased strain magnitudes in the brain. The trend of decreasing swelling with strain was predicted by the nonlinear, time-dependent, partial differential equation developed by Lucantonio et al. (2014) to describe the relationship between one-dimensional swelling of elastomers bonded to an impermeable rigid substrate and the influence of pre-stretch on solvent absorbtion.

Quantifying micromotion reduction using strain as a metric to assess biocompatibility improvement depends on the material model chosen for the finite

element simulations. Lee et al. (2005) modeled the brain tissue as a linear elastic material. However, the literature shows that the brain tissue is viscoelastic (Galford and McElhaney, 1970; Miller and Chinzei, 1997). Thus, finite element simulations were conducted using both the fractional Zener and hyperviscoelastic constitutive model, since these models more closely resemble the viscoelastic behavior of brain tissue (Bentil and Dupaix, 2014; Miller, 1999). The results were compared with the linear elastic description of the brain. Additionally, our research explored the benefit of a hydrogel-coated silicon electrode to reduce micromotion. Lee et al. (2005) considered a brain described by a linear elastic model using an uncoated silicon electrode. The magnitude of micromotion reduction for the FZ, HV, and LE constitutive model differed for strains greater than 5% due to the varying stress-strain relationship. Constitutive models that describe a stiffer brain tissue will encounter less micromotion. For strains less than 5%, the choice of FZ, HV, or LE (Bentil, 2013) constitutive model for a given adhesive condition and coating thickness will yield similar results. Future work will include experiments to determine which constitutive model will best describe micromotion reduction across a range of strains.

For all material models, the electrode coating thickness and the adhesive condition influenced the strain distributions and electrode displacements. Our work has shown that both the maximum principal strains and the maximum electrode displacements can be used as metrics for assessing improvement in the biocompatibility of hydrogel-coated neural electrodes. However, the magnitude of strains and displacements are sensitive to the constitutive model choice. Thus, experiments will be conducted in the future to validate the finite element simulations and quantify the appropriate strain and displacement magnitudes of the implanted hydrogel-coated neural electrodes. Without experimental data, the design guidelines for thickness and stiffness of hydrogel-coated neural electrodes for reduced mechanical mismatch between the brain and electrode will be challenging.

The maximum electrode displacements in FE simulations containing the LE material model (constants from Lee et al. (2005)) for either the brain and/or

hydrogel coating were always lower than the FZ and/or HV constitutive model description for the brain-electrode aggregate. However, earlier work by Bentil (2013) using pig brains suggested that the stiffness at small strains is approximately 9 times smaller than Lee et al. (2005) values. FE simulations using the LE constants from Bentil (2013) yielded larger electrode displacements when compared with Lee et al. (2005) and displacements that were similar to those using the FZ and HV model. This suggests that the smaller maximum electrode displacements obtained using linear elastic constants from Lee et al. (2005) are because of the stiffer material response, and not the type of material model.

The percent difference in electrode displacement due to a 1 μN force boundary condition applied to the uncoated silicon electrode in brain tissue described using the linear elastic constants provided by both Lee et al. (2005) and Bentil (2013) was 88%. This high percent difference was attributed to the Young's modulus of the brain provided by Lee et al. (2005) being 9 times stiffer. To obtain comparable realistic physiological displacements as Lee et al. (2005) in simulations that apply the fractional Zener, hyperviscoelastic, or linear elastic (using Bentil (2013) constants) constitutive models, the force applied to the top of the silicon electrode would need to be decreased by approximately 60%.

A constant material model, adhesive behavior, and hydrogel coating thickness were considered in a finite element simulation to determine the optimal hydrogel coating stiffness that would yield the most strain reduction in the brain. The coating stiffness varied from a value similar to that of native brain tissue to a value that approached the stiffness of the silicon electrode. A coating stiffness that is similar to brain tissue will yield the lowest strains. As the coating becomes stiffer, the strain in the brain increases nonlinearly. The strain magnitudes in the brain due to an implanted coated silicon electrode were lower than the uncoated case, even when the stiffness of the coating was 60 times that of brain tissue. This suggests that having a coating is beneficial at reducing the mechanical mismatch for improved biocompatibility. Application of both a fixed displacement and pressure to the silicon portion of the electrode was examined in the computational study to determine which boundary condition was

effective at capturing the strain changes in the brain due to variable coating stiffness. The fixed displacement condition should be applied in studies that consider variable coating stiffness since the trend for improved biocompatibility in the brain (reduction in strain due to a softer coating) will be the result. Being able to understand the effect of varying stiffness properties is important for electrode coating design. Realistically, the hydrogel coating should be designed such that it is stiff enough to withstand the forces present during the surgical insertion procedure, while avoiding buckling and fracture (Singh et al., 2004). Our simulation results suggest that large strains in the brain would be expected when a stiff hydrogel coating is considered. Following insertion into the cortex, the coating should soften to reduce the strains in the brain attributed to the mechanical mismatch and improve the long term effectiveness of the neural electrode (Jorfi et al., 2015). The aforementioned expectations for the hydrogel coating make it necessary to examine the optimal stiffness value for the hydrogel coating that will lead to a reduction of strain in the brain.

In this work, a fixed displacement boundary condition on the electrode was found to capture the effect of strain reduction with reduced coating stiffness, though it is hypothesized that in an actual application, neither constant displacement nor constant pressure would be seen experimentally. An experimental study is needed in the future to validate the appropriate displacement boundary condition to use for capturing the actual strain bounds that will be present in the brain due to an implanted neural electrode. The displacement from the experimental study will aid in determining the appropriate hydrogel stiffness for optimal strain reduction in the brain tissue. Experiments that examine the influence of electrode adhesion with the brain will also be beneficial for defining the appropriate contact condition in the FE model and understanding the influence of the adhesive case on the chosen constitutive model.

5. Data Availability Statement

All data underlying the findings described in this manuscript is available upon request to the corresponding author.

Acknowledgements

This research was financially supported by the National Science Foundation (NSF) under DGE0221678 and CMMI0747252 and is acknowledged gratefully.

Appendix A. Algorithm for the Fractional Zener (FZ) Constitutive Model to be used in an ABAQUS UMAT File

This appendix summarizes the algorithm for the three-dimensional fractional Zener constitutive model (figure A.1) that was incorporated into the finite element analysis. The UMAT (user defined material) subroutine was written using the programming language FORTRAN. A list of symbols used for implementing the algorithm are described in Appendix A.1. The FZ UMAT algorithm is presented in Appendix A.2.

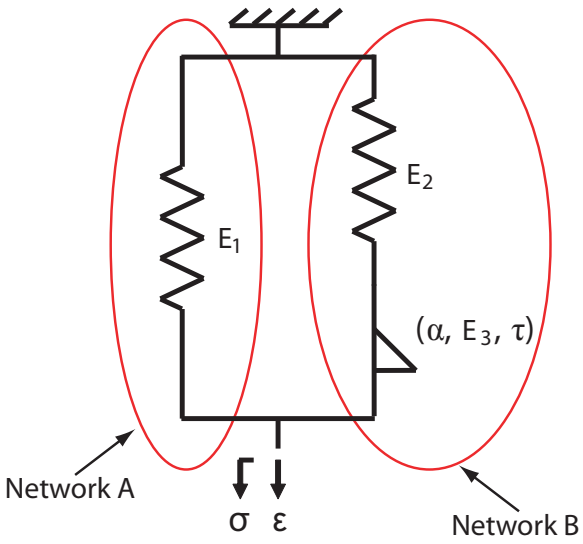

Figure A.1: Fractional Zener constitutive model that was numerical implemented in the finite element package ABAQUS using the UMAT subroutine. Network A represents the linear spring component and Network B describes the fractional Maxwell component.

Appendix A.1. List of Symbols

Symbol	Description
α	Fractional Order
ε	Strain *(scalar)*
$\boldsymbol{\varepsilon}$	Strain *(tensor)*
θ	Specifies the implicitness of the integration in general form*
ν	Poisson's Ratio
σ	Stress *(scalar)*
$\boldsymbol{\sigma}$	Stress *(tensor)*
τ	Relaxation time
$c_j(\alpha)$	Coefficients from truncation of Grünwald's algorithm of differential-integration
$D^{\alpha}(\cdot)$	Fractional derivative operator of order α
d	Fractional Element (Network B)
dev	Deviatoric Part
E	Young's Modulus
e	Elastic Component (Network A)
FM	Fractional Maxwell Component (Network B)
G	Shear Modulus
K	Bulk Modulus
n	Increment Number
vol	Volumetric Part
$\varepsilon^{\mathrm{d}}_{\mathrm{FM,vol}}$	Volumetric component of strain**
Δt	Time Increment
${}^{n}(\cdot)$	Value of the function at time $n\Delta t$
${}^{n+1}(\cdot)$	Value of the function at time $(n+1)\Delta t$
${}^{n}\boldsymbol{\varepsilon}^{-\mathrm{d}}_{\mathrm{FM}}$	Complete viscous strain history***

* $\theta \in (0, 1]$. $\theta = 0.5$ yields the "Classical Midpoint Rule" and $\theta = 1$ is the "Backward Euler Rule".

** Volumetric strain for the fractional element located in the fractional Maxwell component.

*** Strain history is captured by the fractional element in the fractional Maxwell component.

Appendix A.2. Equations for Implementing FZ UMAT

The equations required for implementing the FZ UMAT were adapted from Enelund et al. (1999) and Gil-Negrete et al. (2009). The three-dimensional FZ constitutive model is described as:

$$\begin{aligned}\boldsymbol{\sigma}_{\text{Total}} &= \boldsymbol{\sigma}_{\text{Network A}} + \boldsymbol{\sigma}_{\text{Network B}} \\ &= \boldsymbol{\sigma}_{\text{e}} + \boldsymbol{\sigma}_{\text{FM}}.\end{aligned} \tag{A.1}$$

Decomposition of equation (A.1) into the volumetric part yields:

$$\begin{aligned}\sigma_{\text{vol}} &= \sigma_{\text{e,vol}} + \sigma_{\text{FM,vol}} \\ &= 3K_{\text{e}}\varepsilon_{\text{vol}} + 3K_{\text{FM}}\left(\varepsilon_{\text{vol}} - \varepsilon^{\text{d}}_{\text{FM,vol}}\right),\end{aligned} \tag{A.2}$$

where:

$$K_{\text{e}} = \frac{E_1}{3\left(1-2\nu\right)} \qquad \text{and} \qquad K_{\text{FM}} = \frac{E_2}{3\left(1-2\nu\right)}.$$

Decomposition of equation (A.1) into the deviatoric part yields:

$$\begin{aligned}\boldsymbol{\sigma}_{\text{dev}} &= \boldsymbol{\sigma}_{\text{e,dev}} + \boldsymbol{\sigma}_{\text{FM,dev}} \\ &= 2G_{\text{e}}\boldsymbol{\varepsilon}_{\text{dev}} + 2G_{\text{FM}}\left(\boldsymbol{\varepsilon}_{\text{dev}} - \boldsymbol{\varepsilon}^{\text{d}}_{\text{FM,dev}}\right),\end{aligned} \tag{A.3}$$

where:

$$G_{\text{e}} = \frac{E_1}{2\left(1+\nu\right)} \qquad \text{and} \qquad G_{\text{FM}} = \frac{E_2}{2\left(1+\nu\right)}.$$

Equations (A.2) and (A.3) cannot be numerically evaluated without first integrating equations (A.4) and (A.5) to yield $\varepsilon^{\text{d}}_{\text{FM,vol}}$ and $\boldsymbol{\varepsilon}^{\text{d}}_{\text{FM,dev}}$, respectively.

$$\begin{aligned}\sigma_{\text{vol}} &= \sigma_{\text{e,vol}} + \sigma_{\text{FM,vol}} \\ &= 3K_{\text{e}}\varepsilon_{\text{vol}} + 3b_{\text{vol}}D^{\alpha_{\text{vol}}}\left(\varepsilon^{\text{d}}_{\text{FM,vol}}\right),\end{aligned} \tag{A.4}$$

$$\begin{aligned}\boldsymbol{\sigma}_{\mathrm{dev}} &= \boldsymbol{\sigma}_{\mathrm{e,dev}} + \boldsymbol{\sigma}_{\mathrm{FM,dev}} \\ &= 2G_{\mathrm{e}}\boldsymbol{\varepsilon}_{\mathrm{dev}} + 2b_{\mathrm{dev}} D^{\alpha_{\mathrm{dev}}}\left(\boldsymbol{\varepsilon}^{\mathrm{d}}_{\mathrm{FM,dev}}\right),\end{aligned} \tag{A.5}$$

where:

$$b_{\mathrm{vol}} = \tau^{\alpha_{\mathrm{vol}}} K_{\mathrm{FM}}\left(\frac{E_3}{E_2}\right) \qquad \text{and} \qquad b_{\mathrm{dev}} = \tau^{\alpha_{\mathrm{dev}}} G_{\mathrm{FM}}\left(\frac{E_3}{E_2}\right).$$

The time integration procedure performed in the UMAT, which leads to the numerical solution for the updated stress and strain in Network B, is provided by equations (A.6) and (A.7) for the volumetric component.

$${}^{n+1}\sigma_{\mathrm{FM,vol}} = {}^{n+1}\sigma^{\mathrm{dd}}_{\mathrm{FM,vol}} + c_0 A \Delta\sigma^{\mathrm{de}}_{\mathrm{FM,vol}}, \tag{A.6}$$

$${}^{n+1}\varepsilon^{\mathrm{d}}_{\mathrm{FM,vol}} = \frac{1}{c_0}\left[{}^{n}\varepsilon^{-\mathrm{d}}_{\mathrm{FM,vol}} + \left(\frac{G_{\mathrm{FM}}\left(\Delta t\right)^{\alpha_{\mathrm{vol}}}}{b_{\mathrm{vol}}}\right)\left(\frac{1}{3K_{\mathrm{FM}}}\right)\left(\theta\ {}^{n+1}\sigma_{\mathrm{FM,vol}} + (1-\theta)\ {}^{n}\sigma_{\mathrm{FM,vol}}\right)\right]. \tag{A.7}$$

where:

$$\begin{aligned}
{}^{n+1}\sigma^{\mathrm{dd}}_{\mathrm{FM,vol}} &= A\left[\frac{G_{\mathrm{FM}}\left(\Delta t\right)^{\alpha_{\mathrm{vol}}}}{b_{\mathrm{vol}}}\left(\theta - 1\right) + c_0\right]{}^{n}\sigma_{\mathrm{FM,vol}} + 3K_{\mathrm{FM}} A\left(c_0\, {}^{n}\varepsilon^{\mathrm{d}}_{\mathrm{FM,vol}} - {}^{n}\varepsilon^{-\mathrm{d}}_{\mathrm{FM,vol}}\right), \\
\Delta\sigma^{\mathrm{de}}_{\mathrm{FM,vol}} &= 3K_{\mathrm{FM}}\left(\Delta\varepsilon_{\mathrm{vol}}\right) \\
&= 3K_{\mathrm{FM}}\left({}^{n+1}\varepsilon_{\mathrm{vol}} - {}^{n}\varepsilon_{\mathrm{vol}}\right), \\
A &= \left[\frac{G_{\mathrm{FM}}\left(\Delta t\right)^{\alpha_{\mathrm{vol}}}}{b_{\mathrm{vol}}}\theta + c_0\right]^{-1}, \\
{}^{n}\varepsilon^{-\mathrm{d}}_{\mathrm{FM,vol}} &= -\sum_{j=1}^{n} c_j\left(\alpha_{\mathrm{vol}}\right)^{n+1-j}\varepsilon^{\mathrm{d}}_{\mathrm{FM,vol}}, \\
c_j\left(\alpha_{\mathrm{vol}}\right) &= \left(\frac{j-1-\alpha}{j}\right)c_{j-1}\left(\alpha_{\mathrm{vol}}\right), \\
c_0\left(\alpha_{\mathrm{vol}}\right) &= 1.
\end{aligned}$$

The updated stress and strain in Network B for the deviatoric component is obtained in a similar fashion and is provided by equations (A.8) and (A.9), respectively.

$$ {}^{n+1}\boldsymbol{\sigma}_{\mathrm{FM,dev}} = {}^{n+1}\boldsymbol{\sigma}^{\mathrm{dd}}_{\mathrm{FM,dev}} + c_0 B \Delta\boldsymbol{\sigma}^{\mathrm{de}}_{\mathrm{FM,dev}}, \tag{A.8} $$

$$ {}^{n+1}\boldsymbol{\varepsilon}^{\mathrm{d}}_{\mathrm{FM,dev}} = \frac{1}{c_0}\left[{}^{n}\boldsymbol{\varepsilon}^{-\mathrm{d}}_{\mathrm{FM,dev}} + \left(\frac{G_{\mathrm{FM}}\left(\Delta t\right)^{\alpha_{\mathrm{dev}}}}{b_{\mathrm{dev}}}\right)\left(\frac{1}{2G_{\mathrm{FM}}}\right)\left(\theta\ {}^{n+1}\boldsymbol{\sigma}_{\mathrm{FM,dev}} + \left(1-\theta\right){}^{n}\boldsymbol{\sigma}_{\mathrm{FM,dev}}\right)\right]. \tag{A.9} $$

where:

$$ {}^{n+1}\boldsymbol{\sigma}^{\mathrm{dd}}_{\mathrm{FM,dev}} = B\left[\frac{G_{\mathrm{FM}}\left(\Delta t\right)^{\alpha_{\mathrm{dev}}}}{b_{\mathrm{dev}}}\left(\theta-1\right)+c_0\right]{}^{n}\boldsymbol{\sigma}_{\mathrm{FM,dev}} + 2G_{\mathrm{FM}}B\left(c_0\,{}^{n}\boldsymbol{\varepsilon}^{\mathrm{d}}_{\mathrm{FM,dev}} - {}^{n}\boldsymbol{\varepsilon}^{-\mathrm{d}}_{\mathrm{FM,dev}}\right), $$

$$ \begin{aligned} \Delta\boldsymbol{\sigma}^{\mathrm{de}}_{\mathrm{FM,dev}} &= 2G_{\mathrm{FM}}\left(\Delta\boldsymbol{\varepsilon}_{\mathrm{dev}}\right) \\ &= 2G_{\mathrm{FM}}\left({}^{n+1}\boldsymbol{\varepsilon}_{\mathrm{dev}} - {}^{n}\boldsymbol{\varepsilon}_{\mathrm{dev}}\right), \\ B &= \left[\frac{G_{\mathrm{FM}}\left(\Delta t\right)^{\alpha_{\mathrm{dev}}}}{b_{\mathrm{dev}}}\theta + c_0\right]^{-1}, \\ {}^{n}\boldsymbol{\varepsilon}^{-\mathrm{d}}_{\mathrm{FM,dev}} &= -\sum_{j=1}^{n} c_j\left(\alpha_{\mathrm{dev}}\right)^{n+1-j}\boldsymbol{\varepsilon}^{\mathrm{d}}_{\mathrm{FM,dev}}, \\ c_j\left(\alpha_{\mathrm{dev}}\right) &= \left(\frac{j-1-\alpha}{j}\right)c_{j-1}\left(\alpha_{\mathrm{dev}}\right), \\ c_0\left(\alpha_{\mathrm{dev}}\right) &= 1. \end{aligned} $$

References

ABAQUS, 2011. Version 2011. Dassault Systèmes Simulia Corporation.

Bentil, S.A., 2013. A Fractional Zener Constitutive Model to Describe the Degradation of Swine Cerebrum with Validation from Experimental Data and Predictions using Finite Element Analysis. Doctoral dissertation. The Ohio State University.

Bentil, S.A., Dupaix, R.B., 2014. Exploring the mechanical behavior of degrading swine neural tissue at low strain rates via the fractional zener constitutive model. Journal of the Mechanical Behavior of Biomedical Materials 30, 83–90.

Breit, S., Schulz, J.B., Benabid, A.L., 2004. Deep brain stimulation. Cell and Tissue Research 318, 275–288. Times Cited: 76.

Cheung, K.C., 2007. Implantable microscale neural interfaces. Biomedical Microdevices 9, 923–938. Times Cited: 37.

Cheung, K.C., Renaud, P., Tanila, H., Djupsund, K., 2007. Flexible polyimide microelectrode array for in vivo recordings and current source density analysis. Biosensors & Bioelectronics 22, 1783–1790. Times Cited: 54.

Cutrone, A., Valle, J.D., Santos, D., Badia, J., Filippeschi, C., Micera, S., Navarro, X., Bossi, S., 2015. A three-dimensional self-opening intraneural peripheral interface (seline). Journal of Neural Engineering 12, 016016. URL: http://stacks.iop.org/1741-2552/12/i=1/a=016016, doi:10.1088/1741-2560/12/1/016016.

Davis, G.B., Kohandel, M., Sivaloganathan, S., Tenti, G., 2006. The constitutive properties of the brain paraenchyma part 2. fractional derivative approach. Medical Engineering & Physics 28, 455–459.

Donnelly, B.R., Medige, J., 1997. Shear properties of human brain tissue. Journal of Biomechanical Engineering-Transactions of the Asme 119, 423–432.

Drake, K.L., Wise, K.D., Farraye, J., Anderson, D.J., Bement, S.L., 1988. Performance of planar multisite microprobes in recording extracellular single-unit intracortical activity. IEEE Transactions on Biomedical Engineering 35, 719–732. Times Cited: 187.

Enelund, M., Mahler, L., Runesson, K., Josefson, B.L., 1999. Formulation and integration of the standard linear viscoelastic solid with fractional order rate laws. International Journal of Solids and Structures 36, 2417–2442. Times Cited: 27.

Galford, J.E., McElhaney, J., 1970. A viscoelastic study of scalp, brain, and dura. Journal of Biomechanics 3, 211–221. Times Cited: 98.

Gil-Negrete, N., Vinolas, J., Kari, L., 2009. A nonlinear rubber material model combining fractional order viscoelasticity and amplitude dependent effects. Journal of Applied Mechanics-Transactions of the Asme 76. Times Cited: 0.

Green, R.A., Hassarati, R.T., Goding, J.A., Baek, S., Lovell, N.H., Martens, P.J., Poole-Warren, L.A., 2012. Conductive hydrogels: mechanically robust hybrids for use as biomaterials. Macromolecular bioscience 12.

Green, R.A., Lovell, N.H., Wallace, G.G., Poole-Warren, L.A., 2008. Conducting polymers for neural interfaces: Challenges in developing an effective long-term implant. Biomaterials 29, 3393–3399. ISI Document Delivery No.: 325RS Times Cited: 85 Cited Reference Count: 59 Green, Rylie A. Lovell, Nigel H. Wallace, Gordon G. Poole-Warren, Laura A. Elsevier sci ltd Oxford.

Grill, W.M., Norman, S.E., Bellamkonda, R.V., 2009. Implanted neural interfaces: Biochallenges and engineered solutions. Annual Review of Biomedical Engineering 11, 1–24. Times Cited: 33.

Harris, A.R., Morgan, S.J., Chen, J., Kapsa, R.M.I., Wallace, G.G., Paolini, A.G., 2013. Conducting polymer coated neural recording electrodes. Journal of Neural Engineering 10.

Hassarati, R.T., Dueck, W.F., Tasche, C., Carter, P.M., Poole-Warren, L.A., Green, R.A., 2014. Improving cochlear implant properties through conductive hydrogel coatings. IEEE transactions on neural systems and rehabilitation engineering : a publication of the IEEE Engineering in Medicine and Biology Society 22.

Hetke, J., Anderson, D., 2003. Silicon microelectrodes for extracellular recording, in: Warren E. Finn, P.G.L. (Ed.), Handbook of Neuroprosthetic Methods. CRC Press. number 163-194 in The Biomedical Engineering Series. Doi:10.1201/9781420040876.ch7.

Hochberg, L.R., Serruya, M.D., Friehs, G.M., Mukand, J.A., Saleh, M., Caplan, A.H., Branner, A., Chen, D., Penn, R.D., Donoghue, J.P., 2006. Neuronal ensemble control of prosthetic devices by a human with tetraplegia. Nature 442, 164–171. Accession Number: 16838014. Language: English. Language Code: eng. Date Revised: 20061115. Date Created: 20060713. Date Completed: 20060809. Update Code: 20111122. Publication Type: Journal Article; Research Support, Non-U.S. Gov't. Journal ID: 0410462. Publication Model: Print. Cited Medium: Internet. NLM ISO Abbr: Nature Comment in: Nature. 2006 Jul 13;442(7099):141-2. (PMID: 16838004). Comment in: Nature. 2006 Jul 13;442(7099):109. (PMID: 16837978). Comment in: Nature. 2006 Jul 13;442(7099):125-7. (PMID: 16837993). Linking ISSN: 00280836. Subset: IM. Date of Electronic Publication: 20060713.

JMP, 2015. Version 12. SAS Institute Inc.

Jorfi, M., Skousen, J.L., Weder, C., Capadona, J.R., 2015. Progress towards biocompatible intracortical microelectrodes for neural interfacing applications. Journal of Neural Engineering 12, 011001. URL: http://stacks.iop.org/1741-2552/12/i=1/a=011001, doi:10.1088/1741-2560/12/1/011001.

Kim, D.H., Abidian, M., Martin, D.C., 2004. Conducting polymers grown in hydrogel scaffolds coated on neural prosthetic devices. Journal of Biomedical Materials Research Part A 71A, 577–585. Times Cited: 77.

Kim, D.H., Wiler, J.A., Anderson, D.J., Kipke, D.R., Martin, D.C., 2010. Conducting polymers on hydrogel-coated neural electrode provide sensitive neural recordings in auditory cortex. Acta Biomaterialia 6, 57–62.

Kipke, D.R., Vetter, R.J., Williams, J.C., Hetke, J.F., 2003. Silicon-substrate intracortical microelectrode arrays for long-term recording of neuronal spike activity in cerebral cortex. Ieee Transactions on Neural Systems and Rehabilitation Engineering 11, 151–155. Times Cited: 125 2nd International Meeting on the Brain-Computer Interfaces for Communication and Control Jun, 2002 Rensselaerville, new york.

Lee, H., Bellamkonda, R.V., Sun, W., Levenston, M.E., 2005. Biomechanical analysis of silicon microelectrode-induced strain in the brain. J Neural Eng 2, 81–89.

Lucantonio, A., Nardinocchi, P., Stone, H.A., 2014. Swelling dynamics of a thin elastomeric sheet under uniaxial pre-stretch. Journal of Applied Physics 115, 083505. URL: http://aip.scitation.org/doi/full/10.1063/1.4866576, doi:10.1063/1.4866576.

Maharbiz, M.M., Muller, R., Alon, E., Rabaey, J.M., Carmena, J.M., 2017. Reliable next-generation cortical interfaces for chronic brain-machine interfaces and neuroscience. Proceedings of the IEEE 105, 73–82. doi:10.1109/JPROC.2016.2574938.

Miller, K., 1999. Constitutive model of brain tissue suitable for finite element analysis of surgical procedures. Journal of Biomechanics 32, 531–537. Times Cited: 66.

Miller, K., Chinzei, K., 1997. Constitutive modelling of brain tissue: Experiment and theory. Journal of Biomechanics 30, 1115–1121.

Miller, K., Chinzei, K., 2002. Mechanical properties of brain tissue in tension. Journal of Biomechanics 35, 483–490. Times Cited: 136.

NGC, 2015. National geographic channel successfully concludes first live broadcast of brain surgery from university hospitals case medical center in cleveland, ohio. URL: http://www.businesswire.com/news/home/20151025005050/en/National-Geographic-Channel-Successfully-Concludes-Live-Broadcast.

Polikov, V.S., Block, M.L., Fellous, J.M., Hong, J.S., Reichert, W.M., 2006. In vitro model of glial scarring around neuroelectrodes chronically implanted in the cns. Biomaterials 27, 5368–5376.

Polikov, V.S., Tresco, P.A., Reichert, W.M., 2005. Response of brain tissue to chronically implanted neural electrodes. Journal of Neuroscience Methods 148, 1–18. Times Cited: 241.

Prange, M.T., Margulies, S.S., 2002. Regional, directional, and age-dependent properties of the brain undergoing large deformation. Journal of Biomechanical Engineering-Transactions of the Asme 124, 244–252.

Rao, S., Han, N., Winter, J., 2011. Polylysine-modified peg-based hydrogels to enhance the neuro-electrode interface. Journal Of Biomaterials Science-Polymer Edition 22, 611–625.

Reichert, W., 2008. Indwelling Neural Implants: Strategies for Contending With the in Vivo Environment. Taylor & Francis Group.

Rousche, P.J., Normann, R.A., 1992. A method for pneumatically inserting an array of penetrating electrodes into cortical tissue. Annals of Biomedical Engineering 20, 413–422. Times Cited: 105.

Schendzielorz, P., Scherzed, A., Rak, K., Völker, J., Hagen, R., Mlynski, R., Frölich, K., Radeloff, A., 2014. A hydrogel coating for cochlear implant arrays with encapsulated adipose-derived stem cells allows brain-derived neurotrophic factor delivery. Acta Oto-Laryngologica 134, 497–505. doi:10.3109/00016489.2013.878809.

Singh, A., Zhu, H.X., He, J.P., 2004. Improving mechanical stiffness of coated benzocyclobutene (bcb) based neural implant. Proceedings of the 26th Annual International Conference of the IEEE Engineering in Medicine and Biology Society, Vols 1-7 26, 4298–4301. Times Cited: 1 26th Annual International Conference of the IEEE-Engineering-in-Medicine-and-Biology-Society Sep 01-05, 2004 San Francisco, CA IEEE Engn Med & Biol Soc; Whitaker Fdn; Cyberonics; NIH; NIBIB; NIDOCD; NINDS.

Sridharan, A., Rajan, S.D., Muthuswamy, J., 2013. Long-term changes in the material properties of brain tissue at the implant–tissue interface. Journal of Neural Engineering 10, 066001. URL: http://stacks.iop.org/1741-2552/10/i=6/a=066001, doi:10.1088/1741-2560/10/6/066001.

Subbaroyan, J., Martin, D.C., Kipke, D.R., 2005. A finite-element model of the mechanical effects of implantable microelectrodes in the cerebral cortex. Journal of neural engineering 2, 103–13. Times Cited: 61.

Winter, J.O., Cogan, S.F., Rizzo, Joseph F., I., 2007. Neurotrophin-eluting hydrogel coatings for neural stimulating electrodes. Journal of Biomedical Materials Research Part B-Applied Biomaterials 81B, 551–563. Times Cited: 36.

Xiang, Z., Liu, J., Lee, C., 2016. A flexible three-dimensional electrode mesh: An enabling technology for wireless brain–computer interface prostheses. Microsystems & Nanoengineering 2, 16012. URL: https://www.nature.com/articles/micronano201612, doi:10.1038/micronano.2016.12.

Zhu, R., Huang, G.L., Yoon, H., Smith, C.S., Varadan, V.K., 2011. Biomechanical strain analysis at the interface of brain and nanowire electrodes on a neural probe. Journal of Nanotechnology in Engineering and Medicine 2, 031001–6.